Can we probe the conductivity of the lithosphere and upper mantle using satellite ocean tidal magnetic signals?

by

Neesha Regmi Schnepf

B.S. Science of Earth Systems, Cornell University (2013)

Submitted to the Department of Earth, Atmospheric and Planetary Sciences
in partial fulfillment of the requirements for the degree of

Master of Science

at the

MASSACHUSETTS INSTITUTE OF TECHNOLOGY

June 2015

Signature redacted
Author ....
Department of Earth, Atmospheric and Planetary Sciences
May 15, 2015

Signature redacted
Certified by..
Benjamin P. Weiss
Professor
Thesis Supervisor

Signature redacted
Accepted by..
Robert Van der Hilst
Schlumberger Professor of Earth Sciences, Department Head of Earth, Atmospheric and Planetary Sciences

Can we probe the conductivity of the lithosphere and upper mantle using satellite ocean tidal magnetic signals?

by

Neesha Regmi Schnepf

Submitted to the Department of Earth, Atmospheric and Planetary Sciences
on May 15, 2015, in partial fulfillment of the
requirements for the degree of
Master of Science

Abstract

The 20th century brought many breakthroughs in our understanding of Earth, but there are still many outstanding geophysical questions. Deep electromagnetic studies provide information on electrical conductivity from the near-surface to deep within the mantle (~1600 km) complementing seismic work aiming understand the composition, structure and dynamics of the mantle. Electromagnetic induction studies utilize the skin depth concept which relates the period of a source electromagnetic field and the conductivity of the penetrated material with the maximum depth the field can penetrate. Traditional satellite-based induction studies use signals of magnetospheric origin and considered a period range between a few days and a few months. These traditional studies are mostly sensitive to deep conducting structures because of the inductive coupling between primary and induced sources. In contrast, galvanic coupling from the oceanic tidal signal allows for studying less conductive, shallower structures by also using shorter periods. A few studies convincingly demonstrated that the magnetic fields induced by the lunar semidiurnal ocean tide can be identified in satellite observations. This result encourages using tidal satellite magnetic data to constrain subsurface electrical conductivity in oceanic regions. We perform global 3-D electromagnetic numerical simulations to investigate the sensitivity of the ocean's tidal signals magnetic amplitudes to conductivity distributions at different depths. The results of our sensitivity analysis suggest it will be promising to use oceanic signals detected at satellite altitude for probing lithospheric and upper mantle conductivity. Our simulations also suggest that seafloor electric and magnetic field data may provide complementary details to better constrain lithospheric conductivity.

Thesis Supervisor: Benjamin P. Weiss
Title: Professor

Acknowledgments

I would like to thank my advisors Benjamin P. Weiss and Alexey Kuvshinov for all of their help and guidance. I would also like to thank my other committee members Yuri Sphrits, F. Dale Morgan and John Marshall. Thank you to all members of the MIT Paleomagnetism Lab (Eduardo Lima, Clement Suavet, Sonia Tikoo, Roger Fu, Huapei Wang, Jefferson Ferraz and Rona Oran) and to Christoph Püthe for your help in my various projects. I would also like to thank my co-author Terrence J. Sabaka. A special thank you to Vicki McKenna. And always, I am grateful for the love and support from my family and friends.

This work was supported by my National Science Foundation Graduate Research Fellowship.

Contents

List of Figures

List of Tables

Chapter 1

Introduction

1.1 Overview of ocean electromagnetic fields

In 1832, Michael Faraday was the first to attempt to measure the voltage of flowing water in an experiment he set up in London's Thames river (Faraday, 1832). While not hugely successful, since his work the ocean's electromagnetic fields have been detected by both ground and satellite measurements (Tyler et al., 2003; Maus & Kuvshinov, 2004; Sanford, 1971). While many studies use ocean-bottom magnetometers (Chave et al., 1989; Toh, 1993; Toh et al., 2006; Baba et al., 2010; Schnepf et al., 2014), voltage cables (Larsen & Sanford 1985; Larsen 1991; Thomson et al. 1995; Utada et al. 2003; among others), or coastal stations (McKnight, 1995; Love & Rigler, 2014), using satellite measurements to detect ocean magnetic signals is promising for both Earth (Tyler et al., 2003) and extra-terrestrial applications (Khurana et al., 1998).

The ocean produces electromagnetic fields because it is a conducting fluid with a mean electrical conductivity of $\sigma_{sw} = 3 - 4$ S m^{-1} moving through the Earth's main magnetic field (~50 μT). While the ocean's conductivity is seven orders of magnitude smaller than the conductivity of the copper wires ($\sigma_c = 6.3 \times 10^7$S m^{-1}) we depend on for our electricity, it is still strong enough to induce significant electric fields, currents, and secondary magnetic fields. The ocean's ability to induce electromagnetic fields from the movement of seawater relies on the deflection of electrically charged sea water ions by the Lorentz force perpendicular to the velocity and magnetic field vectors (Tyler et al., 2003):

$$\mathbf{F}_{Lorentz} = q[\mathbf{E} + (\mathbf{v} \times \mathbf{B})] \ , \tag{1.1.1}$$

where q is the charge of the water ions, $\mathbf{v}$ is their velocity and $\mathbf{E}$ and $\mathbf{B}$ are the electric and magnetic fields.

The ocean's magnetic field may be decomposed into two components: the toroidal and poloidal fields. It is estimated that within the ocean the toroidal component reaches amplitudes much larger than the poloidal component, however, it is confined to the ocean and sediments preventing remote observations (Sanford, 1971; Chave & Luther, 1990; Tyler & Mysak, 1995; Tyler et al., 1997, 2003). The toroidal component is a result of electric current circuits forming closed planes containing the vertical axis. Unlike the toroidal component, the poloidal component is much weaker but has a large spatial decay enabling remote observations (Larsen, 1968; Malin, 1970; Bindoff et al., 1988; McKnight, 1995; Tyler et al., 1997, 2003). The poloidal component is formed by horizontally closing electric currents and is less understood since it is generated by large-scale integrals of ocean flow transport requiring large-domain integrations. However, this component's dependency on the flow of ocean water makes these fields useful for gaining information about ocean transport. The information collected in ground and satellite magnetic measurements may be used to study transport quantities in regions that are hard to otherwise access (e.g. the deep ocean or ice covered regions) or from events that may be challenging to monitor, such as tsunamis (Tyler et al., 2003).

1.2 Geomagnetic tides

Tides are periodic oscillations in the Earth-system caused by external celestial forces. Gravitational tides due to the interaction of Earth with the Moon and Sun occur in both the ocean and the atmosphere. Humans have been aware of ocean tides for much of history– the ebb and flow of the sea is easily measured with a shore-side tide gauge

(Hendershott & Munk, 1970; Pugh, 1987)– whereas knowledge of atmospheric tides is relatively newer. Gravitational atmospheric tides can be measured by monitoring surface barometric pressure, but even larger atmospheric tides are caused by the day-side solar heating and night-side cooling (Lindzen & Chapman, 1969).

Oceanic and atmospheric tides are the primary sources of magnetic tides. Tidal gravitational forces cause concurrent motions in the ocean and ionosphere. The tidal waves give rise to motionally induced currents in both the ocean and ionosphere (although the ionosphere's currents are strongest during the day when sunlight is maximal), that then induce secondary currents in the ocean and ionosphere. According to Love & Rigler (2014), in 1882 the director of London's Kew magnetic observatory was the first to speculate that the quiet-time magnetic field variation is due to an electric current in a conducting atmospheric layer and this current somehow relates to the high-altitude winds that are driven by day-night differential heating. This scientist, Stewart, was envisioning what is now known as the ionospheric dynamo: periodic motion of the electrically conducting ionosphere relative to the ambient geomagnetic main field induces electric currents which in turn generate periodic magnetic field variations (Kelley, 1989; Richmond, 1995). These ionospheric currents cause the well known diurnal variations in the geomagnetic field.

Thirty years after Stewart envisioned the ionospheric dynamo, as the director of the Batavia magnetic observatory in Java, van Bemmelen noticed the variation in magnetic field observations corresponded to ocean tides. Due to their periodic nature, the magnetic signals generated by ocean tides are relatively easy to detect and have been studied extensively (Malin, 1970; McKnight, 1995). Using the labels listed by Darwin (1889), Table 1.2 shows the major tidal modes with period near or within a day. Of the gravitational tides, the strongest contributions come from the lunar components. This study chose to focus on three barotropic lunar tides, specifically the lunar semidiurnal (M2), the lunar elliptic semidiurnal (N2), and the lunar diurnal (O1) tidal modes, because they are amongst the strongest lunar tides and resolvable in simulations (Egbert & Erofeeva, 2002; Tyler et al., 2003; Schnepf et al., 2014; Sabaka et al., 2015).

Table 1.1: Reproduced from Love & Rigler (2014)'s Table 1. $1/T = f = \omega/2\pi$.

	Period		Frequency	
$T_\odot$	1.0000 d	$f_\odot$	1.0000/d	Synodic solar day
	0.9973 d		1.0027/d	Sidereal day
$T_{\leftmoon}$	1.0351 d	$f_{\leftmoon}$	0.9661/d	Synodic lunar day
T_m	27.3216 d	f_m	0.0366/d	Sidereal month
	29.5306 d		0.0339/d	Synodic month
T_a	365.2422 d	f_a	1.0000/yr	Tropical year
T_p	8.8475 yr	f_p	0.1130/yr	Sidereal precession of lunar perigee
T_R	~10.4400 yr	f_R	~0.0942/yr	Sunspot solar cycle
T_n	18.6132 yr	f_n	0.0537/yr	Precession of lunar nodes

The many different tidal components (i.e. harmonics) seen in Table 1.2 are due to astronomical observables between the Earth, Moon and Sun (shown in Table 1.1). The different tidal harmonics may be obtained using Fourier representation, for example if ξ is the tidal elevation:

$$\xi(t) = \sum_k C_k(2\pi\mathbf{k}\cdot\mathbf{f}t + \theta_k), \tag{1.2.1}$$

where the tidal constants C_k and θ_k are found by harmonic analysis of the tidal record over many frequencies,

$$\mathbf{k}\cdot\mathbf{f} = k_\odot f_\odot + k_m f_m + k_n f_n + \dots \tag{1.2.2}$$

where $\mathbf{k}$ is known as the Doodson number and $\mathbf{f}$ are the basic frequencies in the motion of the Earth, Moon and Sun (see Table 1.1). The Doodson number is a vector that completely defines the frequency $\mathbf{k}\cdot\mathbf{f}$. In Fourier frequency analysis, each tidal species has three orders of splitting: monthly splitting, a fine structure due to yearly splitting, and a hyperfine structure from lunar perigee and regression (Hendershott & Munk, 1970; Love & Rigler, 2014).

As discussed above, the ocean tidal electromagnetic signals are a combination of the signals produced by both the ocean, ionosphere and induced signal in the solid Earth. To isolate the oceanic tidal fields, the Chapman-Miller method may be used on a complete time series, assuming that the ionospheric tidal signal vanishes

Table 1.2: The periods of different tidal modes and their Fourier constituents (Love & Rigler, 2014). *Indicates the focus tidal modes of this study.

Tide	Period (hour)	Solar k			Lunar k			Secular k		
		⊙	m	a	☾	m	a	p	R	n
S6	4	6	0	0	6	6	-6	0	0	0
S5	4.8	5	0	0	5	5	-5	0	0	0
S4	6	4	0	0	4	4	-4	0	0	0
S3	8	3	0	0	3	3	-3	0	0	0
K2	11.967	2	0	2	2	2	0	0	0	0
S2	12	2	0	0	2	2	-2	0	0	0
M2*	12.421	2	-2	2	2	0	0	0	0	0
N2*	12.658	2	-3	2	2	-1	0	1	0	0
K1	23.934	1	0	1	1	1	0	0	0	0
S1	24	1	0	0	1	1	-1	0	0	0
P1	24.066	1	0	-1	1	1	-2	0	0	0
O1*	25.819	1	-2	1	1	-1	0	0	0	0

at midnight (Malin, 1970). An alternative method is discarding the daytime data and assuming that ionospheric currents are negligible on the night side of the Earth (excluding the high latitudes). The study by Tyler et al. (2003) claimed that the M2 tidal signal can be mapped from *CHAMP* satellite night side measurements. Their mapped signal was largely in agreement with a predicted motionally induced field produced from a satellite radar altimetry based on an ocean flow model (Egbert & Erofeeva, 2002), however it was not until recently that Sabaka et al. (2015) was also successful in isolating the M2 tidal signal from satellite data. Isolating the oceanic tidal signal from satellite data is further discussed in Chapter 2.

While the oceanic tidal signals are 3-4 orders of magnitude weaker than the main magnetic field (less than 10 nT at the sea surface versus 50,000 nT), their persistent nature makes them an important source of noise to remove during geomagnetic field modeling (Maus & Kuvshinov, 2004; Maus et al., 2006). Furthermore, as discussed in below, their proximity to the solid Earth enables them to be a unique source for electromagnetic (EM) sounding.

1.3 Electromagnetic sounding

1.3.1 Motivation for electromagnetic (EM) sounding

The 20th century brought many breakthroughs in our understanding of Earth, but there are still many outstanding geophysical questions: What happens to lithospheric slabs that subduct into the deep mantle? What is the morphology of rising plumes and in what regions of the mantle do they originate? Are there distinct geochemical reservoirs in the mantle? What is the scale and nature of convection in the mantle? Deep electromagnetic (EM) studies provide information on electrical conductivity from the near-surface to deep within the mantle (~1600 km) providing data that complements seismic work aiming to answer these questions and provide a richer understanding of the composition, structure and dynamics of the mantle.

While seismic tomography can recover 3-D variations in seismic wave speed in the mantle (Becker & Lapo, 2002; Romanowicz, 2003), it is unable to separate effects due to compositional versus thermal variations (Trampert et al., 2004; Khan et al., 2009). Instead, electrical conductivity directly relates the temperature and connectivity of constituents as fluids, partial melt, and volatiles– all of which are incredibly important for understanding mantle rheology, convection and tectonic activity. So although geodynamic processes such as mantle convection, the fate of subducting slabs, and the origin of continents all have signatures in seismic wave speed, the general picture of mechanical properties provided by seismic data needs EM sounding to fill in the compositional details (Kuvshinov & Semenov, 2012).

Water in the mantle is a very active area of research because water governs both mineralogical properties, as well as large-scale transport properties such as viscosity and heat flow. Water content is related to material conductivity although how effectively water enhances a given mineral's conductivity is still a controversial area of experimental research. Most experimental research has investigated the effects of water on 1) olivine, the major mineral in the upper mantle (up to ~410 km depth) (Yoshino et al., 2006; Wang et al., 2006), 2) wadsleyite, the major mineral in the upper part of transition zone (abbreviated TZ, has a depth range 410–520 km), and

3) ringwoodite, the major mineral in the lower part of the TZ (520–670 km depth) (Huang et al., 2005; Yoshino et al., 2008; Manthilake et al., 2009; Yoshino et al., 2009). Yoshino et al. (2008) reported that water has little effect on conductivity in both the upper mantle and TZ, whereas Karato & Dai (2009) found the opposite to be the case. The work of Karato & Dai (2009) may be more reliable than that of Yoshino et al. (2008) because they used a broad frequency range to determine the electrical conductivity (see eqn. 1.3.1 below) rather than just using one or two low frequencies (0.1 to 0.01 Hz). Just using a couple low frequencies to probe conductivity introduces systematic bias, however this is still a contentious area.

Wadsleyite and ringwoodite are known to have high water solubility (up to ~3 wt%, Inoue et al. (1995); Kohlstedt et al. (1996)). Additionally, estimates based on planetary accretion models and geochemical mass-balance observations suggest Earth's mantle has a bulk amount of water between three and six Earth ocean masses (Ahrens, 1989; Inoue, 1994). The actual water content in the mantle, especially within the transition zone, is the key parameter to constrain for testing the water filter hypothesis proposed by Bercovici & Karato (2003) (illustrated in Figure 1-1) and for determining the different geochemical origins of mid-ocean ridge basalts (MORBs) and ocean-island basalts (OIBs).

1.3.2 Overview of electromagnetic (EM) sounding

Probing the deep Earth using electromagnetic waves takes advantage of the electromagnetic skin depth concept: a wave of a frequency ω penetrating a medium of conductance σ diminishes in amplitude at a depth δ,

$$\delta = \sqrt{\frac{2}{\mu\omega\sigma}}, \tag{1.3.1}$$

where μ is the magnetic permeability (generally assumed to be that of free space, μ_0). In most EM studies, time series of geomagnetic field vector components undergo a Fourier transform into the frequency domain. The internal and external components of fields due to different frequency waves are then analyzed to produce electrical

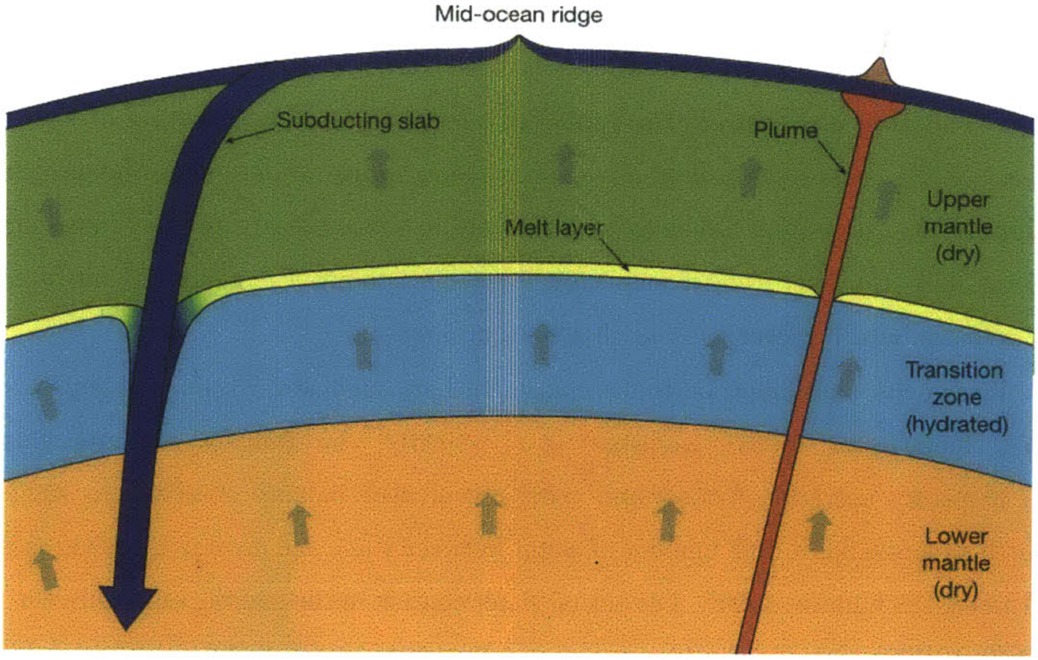

Figure 1-1: Reproduced from Bercovici & Karato (2003), this illustrates the transition-zone water-filter model. Slabs subducting from cold lithosphere (dark blue slabs) force up a broad background of passively upwelling ambient mantle (shaded arrows) that gets hydrated while passing through the high-water-solubility transition zone (light blue region). When leaving the transition zone at the 410-km boundary, this ambient mantle becomes olivine with low-water solubility and is thus supersaturated, wherein it partially melts, thereby extracting water and filtering off incompatible elements into the melt phase. The wet, enriched melt is likely to be heavy and thus gathers into the high-melt fraction layer trapped above the 410-km boundary (yellow layer). The residual solid portion of upwelling ambient mantle is buoyant but very dry and depleted of incompatible elements; it provides the MORB source region (green region). The water-filtering mechanism is suppressed in mantle plumes (red) due to the plume material's higher temperatures and velocities which result in reduced water-solubility and shorter residence times in the transition zone, thereby leading to greatly diminished hydration and thus little or no melting upon passing the 410-km boundary. Plumes thus arrive at the surface still relatively wet and enriched in compatible elements, thereby providing the source for enriched OIBs. Slabs efficiently entrain the melted material, returning water to the transition zone and incompatible elements to the deeper mantle.

conductivity distributions. The period range of the electromagnetic waves used spans from a few hours up to a few years providing a skin depth between 200 to 2,000 km.

The two main sources most frequently used for EM sounding are:

1. Sq variations– the periodic geomagnetic variations caused by the daytime electric currents flowing in the ionosphere (altitude of $\sim$ 110 km). The Sq signal has periods between 4-24 h.
2. Dst variations– the geomagnetic variations caused by modulation of the magnetosphere's ring current. These variations are irregular and have periods longer than one day.

Because these two sources both cause inductive coupling between the source and the Earth's subsurface, they are more sensitive to the deeper, more conductive regions of the Earth. Instead of using these atmospheric sources, using oceanic tides utilizes direct galvanic coupling between the ocean's electric currents and the lithosphere/upper-mantle (LUM) enabling shallower EM sounding. Galvanic coupling differs from inductive coupling because the conductive materials are touching so a variational electric field is induced in the Earth and an electric current flows in the subsurface. Magnetic ocean tides produce an electric field and electric current in the substrate directly beneath the oceans enabling probing the conductivity in regions too resistive for inductive coupling. Furthermore, while the Sq and Dst variations are both a global source, the signal from oceanic tides is localized to oceanic regions enabling higher accuracy EM sounding of oceanic LUM.

The recent expansion in high-accuracy global geomagnetic data from low-Earth orbiting (LEO) satellite missions (Oersted, CHAMP, SAC-C and *Swarm*) has led to a rising interest in using these satellites to produce global conductivity-depth profiles (see Kuvshinov & Olsen 2006; Velímský 2010; Püthe et al. 2015). In fact, mapping the three-dimensional (3-D) electrical conductivity of Earth's mantle and producing a data-based model describing Earth's 3-D electrical conductivity are two of the main scientific objectives of *Swarm* (Olsen et al., 2013). There are many benefits to using satellite missions rather than ground-based observatories, the largest being much improved spatial coverage with high-precision data of uniform quality. However, as discussed further in Chapter 2, the process of inverting satellite magnetometer data to produce conductivity models is a non-trivial task: LEO satellites typically move with speeds of 7-8 km/s and measure a superposition of temporal and spatial geomagnetic field changes.

To date, all satellite-based EM sounding studies have used time-varying magnetic fields of magnetospheric origin. In this study, we investigate the sensitivity of oceanic magnetic tides for satellite-based EM sounding and attempt inversions of data for LUM conductivity profiles. While oceanic tidal magnetic signals can be most easily detected either at seafloor (Kuvshinov et al., 2006; Schnepf et al., 2014) or at coastal stations (Maus & Kuvshinov, 2004; Love & Rigler, 2014), the studies by Tyler et al. (2003) and Sabaka et al. (2015) isolated the magnetic signals produced by the lunar semidiurnal (M2) ocean tide from CHAMP, SAC-C and Oersted nighttime data. The M2 tidal mode is the only tidal mode that can so far be reliably extracted from satellite data thus limiting resolution in the radial direction. Despite this, the advantages of using tidal signals to probe Earth's interior render it worthy of investigation.

Note that because we are only discussing M2, N2 and O1 tidal signals, this is different than EM sounding studies where the aim is to determine conductivity as a function of different frequencies. Considering a) the long period of M2 (12.421 hours), N2 (12.658 hours) and O1 (25.819 hours) variations ; b) the galvanic excitation of the Earth from the oceanic tidal currents and c) the rich spatial content of the oceanic tidal sources (cf. Figure 11 in Sabaka et al. 2015 for M2), this type of Earth-probing is a form of geoelectric sounding analogous with the direct current (DC) electric sounding method. The latter method is based on DC or low frequency current injection through grounded electrodes (galvanic excitation). It is known that the depth of DC sounding depends on the distance between the electrodes. In the case of oceanic tides, the different spatial scales of the tidal source may be related to the different distances between electrodes in DC sounding. This enables sensing conductivity at different depths (Schnepf et al., 2015).

1.3.3 Comparing EM and seismic tomography

As previously stated, electromagnetic sounding provides additional constraints from seismic studies enabling further determination of the temperature and composition of the mantle. As shown in Figure 1-2, both electrical conductivity and seismic velocity vary with depth, however they are each dependent on different parameters (for example, bulk material properties versus chemical composition).

Fukao et al. (2004) conducted the first study synthesizing transition zone temperature anomaly images from seismic and electromagnetic (EM) tomography. Their EM tomography utilized submarine geopotential cables in the Pacific Ocean and their seismic tomography was produced from the arrivals and broadband PP-P times. A rendition of their results is shown in Figure 1-3 where the first column represents P-waves, the second column S-waves and the third column represents electrical conductivity. Each row relates an increase in depth. Looking across the plots, it is apparent that there are not large anomalies of P-waves, but larger S-wave anomalies occur near Hawaii and Japan. At 400-500 km depth, the largest anomaly in electrical conductivity occurs in the Philippine Sea (denoted with a bold box). There are no similar seismic anomalies in this area, instead the seismic tomography indicates that this anomaly is due to cold slabs stagnant beneath the region (Fukao et al., 2004).

As shown in Figure 1-4, a temperature-depth profile may be inferred from both seismic and EM tomographic data. Seismic speeds are related to temperature via

$$dT_{3D} = -c\frac{\mathrm{dV}_{3\mathrm{D}}}{V_{1D}}, \tag{1.3.2}$$

where dT_{3D} is the lateral temperature perturbation from the radially symmetric temperature distribution T_{1D} and dV_{3D} is the lateral velocity perturbation from the radially symmetric velocity distribution V_{1D}. Conductivity may be converted to temperature using

$$\frac{dT_{3D}}{T_{1D}} = -\frac{\ln(\sigma_{3D}/\sigma_{1D})}{\ln(\sigma_{1D}/\sigma_0)}, \tag{1.3.3}$$

where σ_{1D} is the radially symmetric conductivity model used as a starting model for

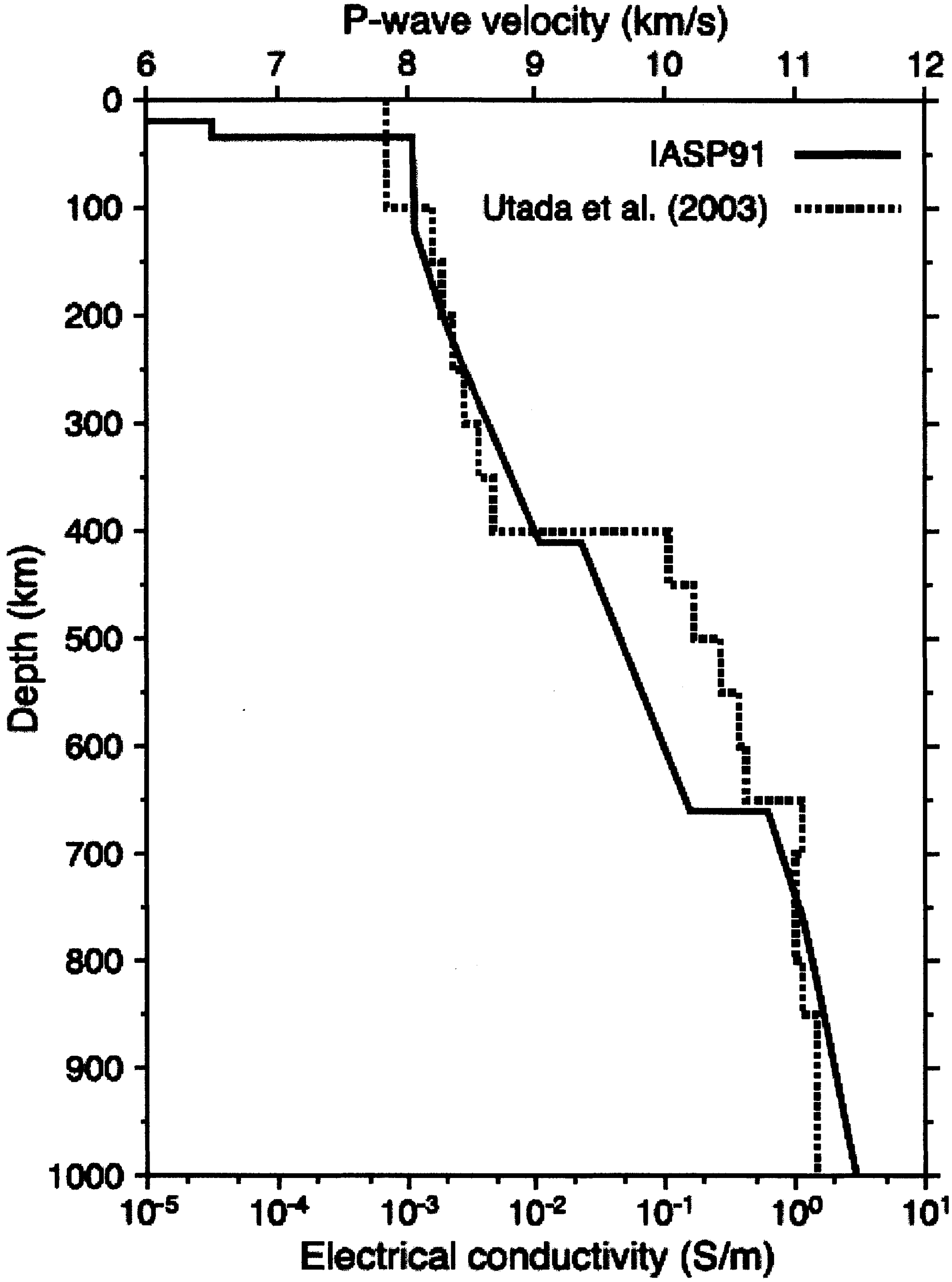

Figure 1-2: Reproduced from Fukao et al. (2004), this shows the general understanding of how P-wave velocity (Kennett & Engdahl, 1991) and electrical conductivity (Utada et al., 2003) vary with depth. The scale for the P-wave is linear whereas that for conductivity is logarithmic.

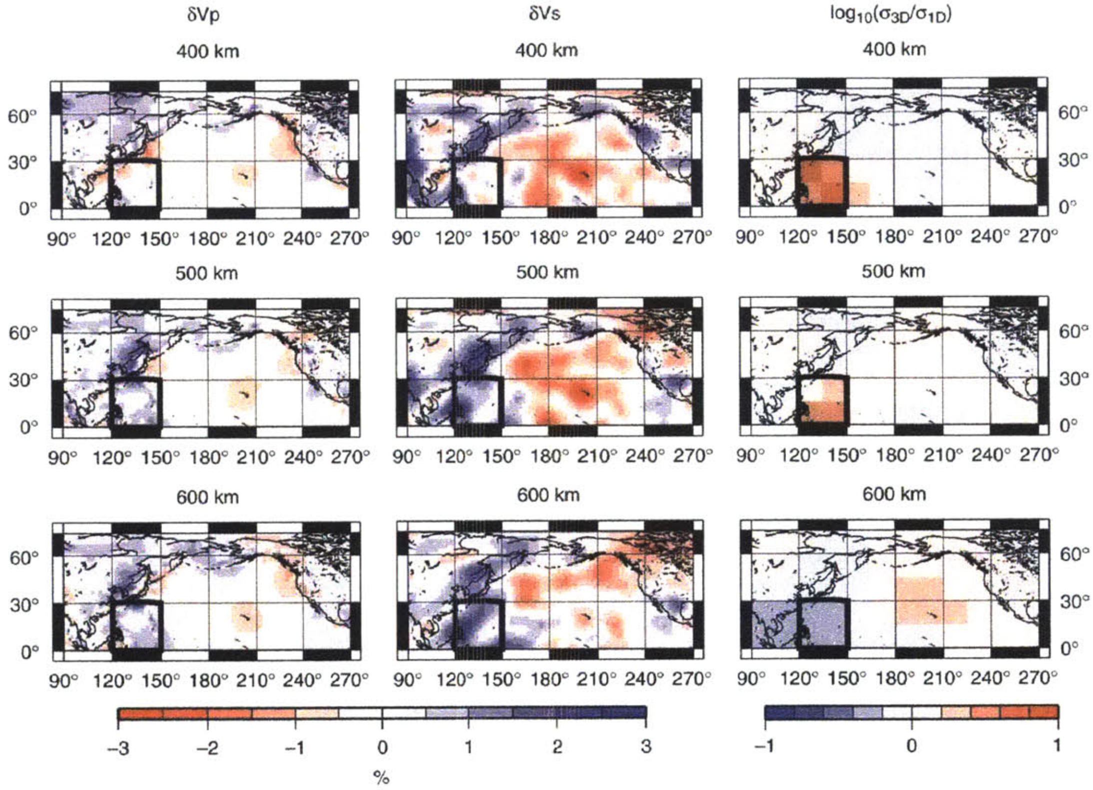

Figure 1-3: Reproduced from Utada et al. (2009) but based on the results from Fukao et al. (2004), this is a comparison of P-wave, S-wave and EM tomography at depths of 400, 500 and 600 km in the Pacific. The bold box indicates a high-conductivity anomaly in the Philippine Sea; note that there is no apparent accompanying velocity anomaly.

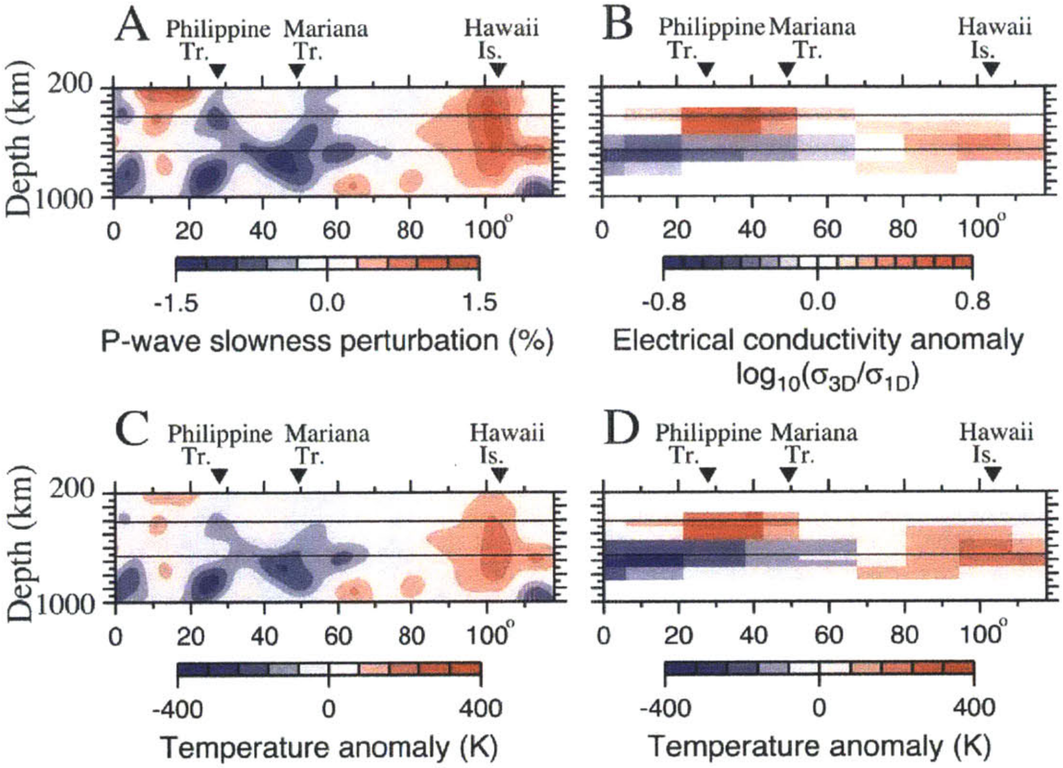

Figure 1-4: Reproduced from Fukao et al. (2004), this shows cross-sections of the mantle beneath the Pacific Ocean between Hawaii and the Philippines. A) P-wave velocity anomalies between 200-1000 km depth. B) Electrical conductivity anomalies between 350-850 km depths. C) Temperature anomalies converted from P-wave velocity anomalies. D) Temperature anomalies converted from electrical conductivity anomalies.

inversion for the three-dimensional conductivity model σ_{3D}. σ_0 is the pre-exponential term of the mantle mineral Arrhenius formula for the relevant depth range:

$$\sigma = \sigma_0 \exp\left(-\frac{H}{kT}\right), \tag{1.3.4}$$

where H is the activation enthalpy and k is Boltzmann's constant. Fukao et al. (2004) used the geometric mean of σ_0 laboratory values for wadsleyite and ringwoodite from Xu et al. (1998). In general, they found good agreement between the temperatures found from conductivity and seismic data. The cold anomaly in Fig. 1-4A and Fig. 1-4C corresponds to a cold subducting slab. In general, EM tomography is more sensitive to hot (more conductive) anomalies and less sensitive to cold (more resistive) anomalies compared to seismic tomography.

1.4 Thesis goals

The goal of this thesis is to use the ocean tidal magnetic signal extracted from satellite data (discussed in Ch. 2) and produced from simulations to determine the sensitivity of ocean tidal magnetic signals to the conductivity of different layers of the lithosphere and upper mantle (Ch. 3). A summary of the results and conclusions for the future is given in Ch. 4.

1.5 References

Ahrens, T. J., 1989. Water storage in the mantle, *Nature*, **342**, 122–123.

Baba, K., Utada, H., Goto, T.-N., Kasaya, T., Shimizu, H., & Tada, N., 2010. Electrical conductivity imaging of the Philippine Sea upper mantle using seafloor magnetotelluric data, *Physics of the Earth and Planetary Interiors*, **183**(1-2), 44–62.

Becker, T. W. & Lapo, B., 2002. A comparison of tomographic and geodynamic mantle models, *Geochemistry Geophysics Geosystems*, **3**.

Bercovici, D. & Karato, S.-I., 2003. Whole-mantle convection and the transition-zone water filter., *Nature*, **425**, 39–44.

Bindoff, N. L., Lilley, F. E. M., & Filloux, J. H., 1988. A separation of ionospheric and ocean tidal components in magnetic fluxuation data, *Journal of geomagnetism and geoelectricity*, **40**, 1445–1467.

Chave, A. D. & Luther, D. S., 1990. Low-Frequency, Motionally Induced Electromagnetic Fields in the Ocean. 1. Theory, *Journal of Geophysical Research*, **95**(C5), 7185–7200.

Chave, A. D., Filloux, J. H., & Luther, D. S., 1989. Electromagnetic induction by ocean currents: BEMPEX, *Physics of the Earth and Planetary Interiors*, **53**(3-4), 350–359.

Darwin, G. H., 1889. Second series of results of the harmonic analysis of tidal observations, *Proceedings of the Royal Society of London*, **45**, 556–611.

Egbert, G. D. & Erofeeva, S. Y., 2002. Efficient Inverse Modeling of Barotropic Ocean Tides, *Journal of Atmospheric and Oceanic Technology*, **19**, 183–204.

Faraday, M., 1832. The Bakerian Lecture. Experimental Researches in Electricity. Terrestrial Magneto-electric Induction., *Philosophical Transactions of the Royal Society of London*, **122**, 163–194.

Fukao, Y., Koyama, T., Obayashi, M., & Utada, H., 2004. Trans-Pacific temperature field in the mantle transition region derived from seismic and electromagnetic tomography, *Earth and Planetary Science Letters*, **217**, 425–434.

Hendershott, M. & Munk, W., 1970. Tides, *Annual Reviews*, **2**, 1–19.

Huang, X., Xu, Y., & Karato, S.-I., 2005. Water content in the transition zone from electrical conductivity of wadsleyite and ringwoodite., *Nature*, **434**, 746–749.

Inoue, T., 1994. Effect of water on melting phase relations and melt composition in the system Mg2SiO4-MgSiO3-H2O up to 15 GPa, *Physics of the Earth and Planetary Interiors*, **85**(94), 237–263.

Inoue, T., Yurimoto, H., & Kudoh, Y., 1995. Hydrous modified spinel, Mg1.75SiH0.5O4: A new water reservoir in the mantle transition region, *Geophysical Research Letters*, **22**(2), 117.

Karato, S. I. & Dai, L., 2009. Comments on "Electrical conductivity of wadsleyite as a function of temperature and water content" by Manthilake et al., *Physics of the Earth and Planetary Interiors*, **174**, 19–21.

Kelley, M. C., 1989. *The Earth's Ionosphere: Plasma Physics and Electrodynamics*, Academic Press Inc.

Kennett, B. L. N. & Engdahl, E. R., 1991. Traveltimes for global earthquake location and phase identification, *Geophysical Journal International*, **105**(2), 429–465.

Khan, A., Boschi, L., & Connolly, J. A. D., 2009. On mantle chemical and thermal heterogeneities and anisotropy as mapped by inversion of global surface wave data, *Journal of Geophysical Research: Solid Earth*, **114**, 1–21.

Khurana, K. K., Kivelson, M. G., Stevenson, D. J., Schubert, G., Russell, C. T., Walker, R. J., & Polanskey, C., 1998. Induced magnetic fields as evidence for subsurface oceans in Europa and Callisto, *Nature*, **395**(October), 777–780.

Kohlstedt, D. L., Keppler, H., & Rubie, D. C., 1996. Solubility of water in the α, β and γ phases of (Mg,Fe)2SiO4, *Contributions to Mineralogy and Petrology*, **123**, 345–357.

Kuvshinov, A. & Olsen, N., 2006. A global model of mantle conductivity derived from 5 years of CHAMP, Ørsted, and SAC-C magnetic data, *Geophysical Research Letters*, **33**(18), L18301.

Kuvshinov, A. & Semenov, A., 2012. Global 3-D imaging of mantle electrical conductivity based on inversion of observatory C-responses-I. An approach and its verification, *Geophysical Journal International*, **189**, 1335–1352.

Kuvshinov, A., Junge, A., & Utada, H., 2006. 3-D modelling the electric field due to ocean tidal flow and comparison with observations, *Geophysical Research Letters*, **33**(6), L06314.

Larsen, J. C., 1968. Electric and Magnetic Fields Induced by Deep Sea Tides, *The Geophysical Journal of the Royal Astronomical Society*, **16**, 47–70.

Larsen, J. C., 1991. Transport measurements from in-service undersea telephone cables, *IEEE Journal of Oceanic Engineering*, **16**(4), 313–318.

Larsen, J. C. & Sanford, T. B., 1985. Florida current volume transports from voltage measurements, *Science*, **227**(4684), 302–304.

Lindzen, R. S. & Chapman, S., 1969. Atmospheric tides, *Space Sci. Rev*, **10**, 3–188.

Love, J. J. & Rigler, E. J., 2014. The magnetic tides of Honolulu, *Geophysical Journal International*, **197**, 1335–1353.

Malin, S. R. C., 1970. Separation of lunar daily geomagnetic variations into parts of ionospheric and oceanic origin., *The Geophysical Journal of the Royal Astronomical Society*, **21**, 447–455.

Manthilake, M. A. G. M., Matsuzaki, T., Yoshino, T., Yamashita, S., Ito, E., & Katsura, T., 2009. Electrical conductivity of wadsleyite as a function of temperature and water content, *Physics of the Earth and Planetary Interiors*, **174**, 10–18.

Maus, S. & Kuvshinov, A., 2004. Ocean tidal signals in observatory and satellite magnetic measurements, *Geophysical Research Letters*, **31**, L15313.

Maus, S., Rother, M., Stolle, C., Mai, W., Choi, S., Lühr, H., Cooke, D., & Roth, C., 2006. Third generation of the Potsdam Magnetic Model of the Earth (POMME), *Geochemistry, Geophysics, Geosystems*, **7**, 1–9.

McKnight, J. D., 1995. Lunar daily geomagnetic variations in New Zealand, *Geophysical Journal International*, **122**, 889–898.

Olsen, N., Friis-Christensen, E., Floberghagen, R., Alken, P., Beggan, C. D., Chulliat, A., Doornbos, E., Da Encarnação, J. a. T., Hamilton, B., Hulot, G., Van Den Ijssel, J., Kuvshinov, A., Lesur, V., Lühr, H., Macmillan, S., Maus, S., Noja, M., Olsen, P. E. H., Park, J., Plank, G., Püthe, C., Rauberg, J., Ritter, P., Rother, M., Sabaka, T. J., Schachtschneider, R., Sirol, O., Stolle, C., Thébault, E., Thomson, A. W. P., Tø ffner Clausen, L., Velímský, J., Vigneron, P., & Visser, P. N., 2013. The Swarm satellite constellation application and research facility (SCARF) and Swarm data products, *Earth, Planets and Space*, **65**(c), 1189–1200.

Pugh, D. T., 1987. *Tides, surges and mean sea-level*, John Wiley & Sons.

Püthe, C., Kuvshinov, A., Olsen, N., & Khan, A., 2015. A new model of Earth's radial conductivity structure derived from over 10 years of satellite and observatory magnetic data, *submitted to Geophysical Journal International*.

Richmond, A. D., 1995. Modeling equatorial ionospheric electric field, *Journal of Atmospheric and Terrestrial Physics*, **57**, 1103–1115.

Romanowicz, B., 2003. Global mantle tomography: progress status in the past 10 years, *Annual Review of Earth and Planetary Sciences*, **31**, 303–328.

Sabaka, T. J., Olsen, N., Tyler, R. H., & Kuvshinov, a., 2015. CM5, a pre-Swarm comprehensive geomagnetic field model derived from over 12 yr of CHAMP, Orsted, SAC-C and observatory data, *Geophysical Journal International*, **200**, 1596–1626.

Sanford, T. B., 1971. Motionally induced electric and magnetic fields in the sea, *Journal of Geophysical Research*, **76**(15).

Schnepf, N. R., Manoj, C., Kuvshinov, A., Toh, H., & Maus, S., 2014. Tidal signals in ocean bottom magnetic measurements of the Northwestern Pacific: Observation versus prediction, *Geophysical Journal International*, **198**(2), 1096–1110.

Schnepf, N. R., Kuvshinov, A., & Sabaka, T. J., 2015. Can we probe the conductivity of the lithosphere and upper mantle using satellite tidal magnetic signals?, *Geophysical Research Letters*.

Thomson, D. J., Lanzerotti, L. J., Maclennan, C. G., & Medford, L. V., 1995. Ocean cable measurements of the tsunami signal from the 1992 Cape Mendocino earthquake, *Pure and Applied Geophysics*, **144**(3-4), 427–440.

Toh, H., 1993. *Electrical conductivity structure of the Izu-Bonin arc revealed by seafloor electromagnetic observation*, Ph.D. thesis, University of Tokyo, Tokyo, Japan.

Toh, H., Hamano, Y., & Ichiki, M., 2006. Long-term seafloor geomagnetic station in the northwest Pacific : A possible candidate for a seafloor geomagnetic observatory, *Earth Planets Space*, **58**, 697–705.

Trampert, J., Deschamps, F., Resovsky, J., & Yuen, D., 2004. Probabilistic tomography maps chemical heterogeneities throughout the lower mantle., *Science*, **306**, 853–856.

Tyler, R. H. & Mysak, L. A., 1995. Motionally-induced electromagnetic fields generated by idealized ocean currents, *Geophysical and Astrophysical Fluid Dynamics*, **80**(3-4), 167–204.

Tyler, R. H., Sanford, T. B., & Oberhuber, J. M., 1997. Geophysical Challenges in Using Large-Scale Ocean-Generated EM Fields to Determine the Ocean Flow, *Journal of geomagnetism and geoelectricity*, **49**(11), 1351–1372.

Tyler, R. H., Maus, S., & Lühr, H., 2003. Satellite observations of magnetic fields due to ocean tidal flow., *Science*, **299**(5604), 239–241.

Utada, H., Koyama, T., Shimizu, H., & Chave, A. D., 2003. A semi-global reference model for electrical conductivity in the mid-mantle beneath the north Pacific region, *Geophysical Research Letters*, **30**(4), 2–5.

Utada, H., Koyama, T., Obayashi, M., & Fukao, Y., 2009. A joint interpretation of electromagnetic and seismic tomography models suggests the mantle transition zone below Europe is dry, *Earth and Planetary Science Letters*, **281**(3-4), 249–257.

Velímský, J., 2010. Electrical conductivity in the lower mantle: Constraints from CHAMP satellite data by time-domain EM induction modelling, *Physics of the Earth and Planetary Interiors*, **180**, 111–117.

Wang, D., Mookherjee, M., Xu, Y., & Karato, S.-i., 2006. The effect of water on the electrical conductivity of olivine, *Nature*, **443**(October), 977–980.

Xu, Y., Poe, B. T., Shankland, T. J., & Rubie, D. C., 1998. Electrical conductivity of olivine, wadsleyite and ringwoodite under upper-mantle conditions, *Science*, **280**, 1415–1418.

Yoshino, T., Matsuzaki, T., Yamashita, S., & Katsura, T., 2006. Hydrous olivine unable to account for conductivity anomaly at the top of the asthenosphere., *Nature*, **443**(October), 973–976.

Yoshino, T., Manthilake, G., Matsuzaki, T., & Katsura, T., 2008. Dry mantle transition zone inferred from the conductivity of wadsleyite and ringwoodite., *Nature*, **451**(January), 326–329.

Yoshino, T., Matsuzaki, T., Shatskiy, A., & Katsura, T., 2009. The effect of water on the electrical conductivity of olivine aggregates and its implications for the electrical structure of the upper mantle, *Earth and Planetary Science Letters*, **288**, 291–300.

Chapter 2

Satellite data

2.1 Satellite magnetic fields

Geomagnetic field investigations are typically done in the pre-Maxwell quasi-static approximation which requires that the considered time scales are longer ($\gg 1$s) compared to the time required for light to pass the length scale of interest (which is less than a few thousand km). In this approximation, displacement currents can be neglected so the magnetic field $\mathbf{B}$ is given by

$$\nabla \times \mathbf{B} = \sigma \mathbf{E} + j^{ext}, \tag{2.1.1}$$

where $\mu_0 = 4\pi \times 10^{-7}$ Vs(Am)$^{-1}$ is the vacuum permeability and j^{ext} is the excited current density (A/m^2). As shown in Fig. 2-1, there are many different electric current sources, those on or within the Earth's surface are considered internal sources and those in the atmosphere or near-Earth space are external sources.

Outside the external source and in an insulating atmosphere (eqn. 2.1.1) degenerates to $\nabla \times \mathbf{B} = 0$ and thus $\mathbf{B}$ can be represented as $\mathbf{B} = -\nabla V$. Then using

$$\nabla \cdot \mathbf{B} = 0, \tag{2.1.2}$$

one can obtain the Laplacian equation for V: $\Delta V = 0$. The solution of the latter can

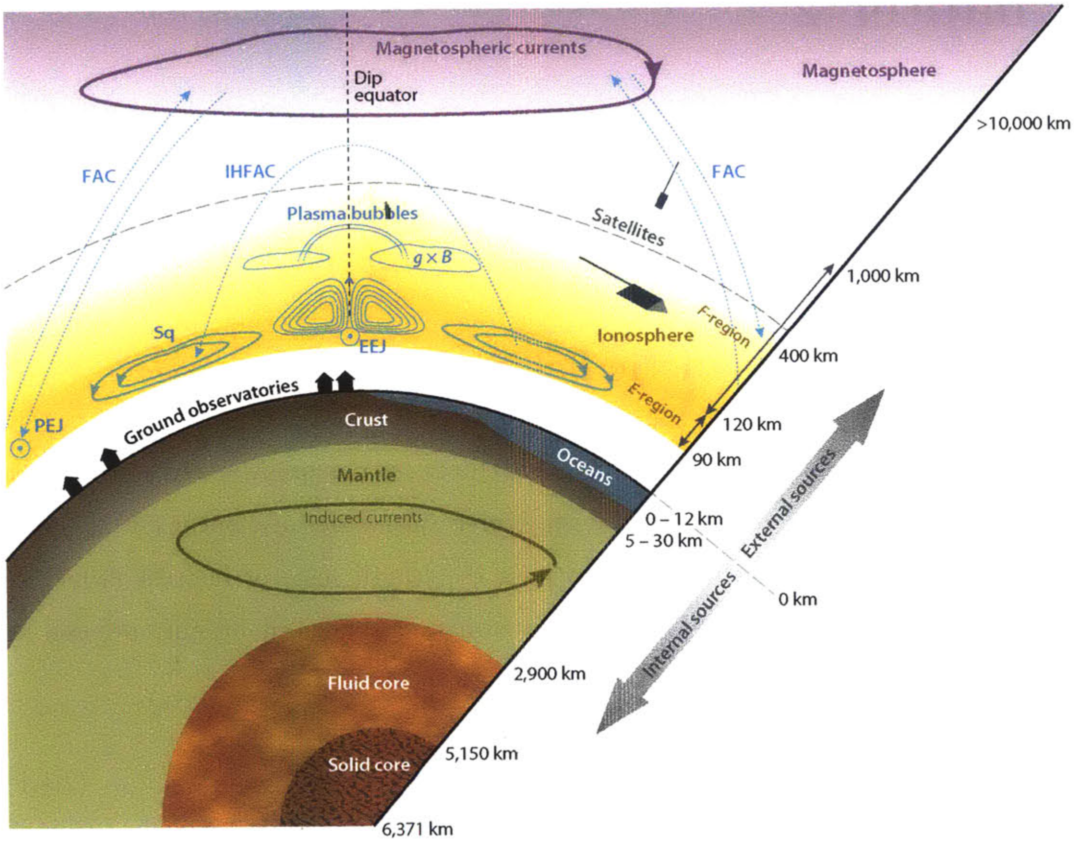

Figure 2-1: Reproduced from Olsen & Stolle (2012), this figure illustrates the internal and external geomagnetic field sources. Abbreviations: **B**, ambient magnetic field; EEJ, equatorial electrojet; FAC, field-aligned current; **g**, Earth's gravity vector; IHFAC, interhemispheric field-aligned current; PEJ, polar electrojet; Sq, solar quiet daily magnetic variation.

be represented in the form of

$$V = V^{int} + V^{ext} = a \sum_{n=1}^{N_{int}} \sum_{m=0}^{n} (g_n^m \cos m\phi + h_n^m \sin m\phi) \left(\frac{a}{r}\right)^{n+1} P_n^m(\cos\theta)$$
$$+ a \sum_{n=1}^{N_{ext}} \sum_{m=0}^{n} (q_n^m \cos m\phi + s_n^m \sin m\phi) \left(\frac{r}{a}\right)^{n} P_n^m(\cos\theta), \quad (2.1.3)$$

where a is the reference Earth radius (6371.2 km), (r, θ, ϕ) are spherical coordinates, P_n^m are the associated Schmidt semi-normalized Legendre functions, N_{int} is the maximum degree of the expansion (Gauss) coefficients g_n^m, h_n^m describing internal sources and N_{ext} is that for the coefficients q_n^m, s_n^m describing external sources. Analyzing the horizontal and vertical magnetic field components allows determination of g_n^m, h_n^m and q_n^m, s_n^m, enabling separation of internal and external sources.

In reality, satellites move through the ionosphere's plasma so electric currents do exist at satellite altitude. The toroidal magnetic field produced by the in-situ electric currents is mathematically orthogonal to the Laplacian potential field caused by internal and external sources (which are poloidal fields). With proper data sampling, the toroidal magnetic field has minimal impact on the determination of the potential field (Olsen & Kotsiaros, 2011).

The main challenge of using satellite data is that it is not possible to decide whether an observed magnetic field variation is due to a temporal or spatial change because the satellite travels with a velocity of $\sim$ 8 km/s at an altitude of 400+ km. However, the benefits of using satellite data encourage coping with this difficulty: 1) satellites map the entire Earth (apart from a polar gap if the orbit inclination is $\neq 90°$), 2) the observations are taken over different regions using the same magnetometer minimizing the spurious effects due to different instrumentation, and 3) a spatially low-pass-filtered magnetic field map with reduced influence of local magnetic heterogeneities is produced because taking measurements at an altitude of at least 400 km corresponds to averaging over an area of this dimension (Olsen & Kotsiaros, 2011; Kuvshinov, 2012).

Before GPS, error in satellite position (especially in the radial direction) was

Table 2.1: Recent satellite magnetometer missions (Olsen & Kotsiaros, 2011).

Mission	Operation	Inclination	Altitude (km)	Data
Øersted	Feb 23 1999 –	97°	650–850	scalar and vector
SAC-C	Jan 2001 – Dec 2004	97°	698-0705	scalar only
CHAMP	July 2000 – 2010	86°	310–450	scalar and vector
Swarm	Nov 22 2013 – 2016	87°/88°	<450–530	scalar and vector

the main source of data error. The situation has dramatically improved with GPS limiting time errors to less than a few ms and spatial errors to less than a few meters. A timing error of 5 ms corresponds to an along-track position error of 40 m which causes a magnetic field error of less than 0.5 nT. For satellite missions such as Ørested, CHAMP and *Swarm*, the contribution of position and timing errors to the overall magnetic error budget is well below 1 nT (Olsen & Kotsiaros, 2011).

2.2 Satellite data processing

2.2.1 Data calibration and alignment

Magnetic signals from the M2 ocean tide have been successfully detected from the Øersted, SAC-C and CHAMP missions' magnetometer data (see Table 2.1). This section provides an overview of extracting the tidal signals from satellite data.

Data calibration Raw vector magnetometer readings are converted into scaled magnetic field components (units of nT) in the orthogonal coordinate system. Satellite vector magnetometers are fluxgate instruments that are calibrated in-orbit by comparing the instrument readings with the magnetic field intensity measured simultaneously by an absolute scalar magnetometer (generally an Overhauser instrument). Details of the in-flight calibration may be found in Olsen et al. (2003).

Data alignment Data alignment is needed to merge the calibrated vector data with attitude data and then transform them to spherical vector components in an Earth-Centered-Earth-Fixed (ECEF) coordinate system. The rotation (Euler) angles between the star imager and the vector magnetometer must be precisely determined utilizing models of star constellations and the ambient magnetic field. Star positions are known with high precision, so the limiting factor in this process is the accuracy of the ambient magnetic field at each time and position data point. This differs from the alignment of ground observatory data where the ambient field may be more easily estimated by simply turning the magnetometer 180° and taking additional measurements (Olsen & Kotsiaros, 2011). More details on data alignment may be found in Olsen et al. (2003).

2.2.2 The comprehensive magnetic field model (CM5)

The study of Tyler et al. (2003) claimed to isolate M2 tidal magnetic signals from CHAMP nightside data and since then many groups tried, and failed, to reproduce their results. Finally, the work of Sabaka et al. (2015) also succeeded in isolating oceanic M2 magnetic signals from satellite data. Their work utilized the comprehensive magnetic field model (CM5) which was derived from CHAMP, Ørsted and SAC-C satellite nightside data, as well as ground observatory data hourly-means from August 2000 to January 2013. Figure 2-2 shows the total measurements from each observatory used in CM5 (top figure) and the total measurements from geomagnetic quiet periods (bottom figure). The Kp and D_{st} indices were used to determine geomagnetic quiet periods. The Kp index measures planetary-scale magnetic activity and is derived from 13 sub-auroral observatories in a manner that compensates for diurnal and seasonal variations.The D_{st} index is an equatorial storm index determined from low-latitude observatories so it relates the activity of the magnetospheric ring current. For non-polar regions (latitude spanning from the equator to ±60°), data was considered quiet if the geomagnetic activity index $Kp \leq 2^{\circ}$ and if the D_{st} index does not change by more than 2 nT hr^{-1}. For polar regions (latitude greater than 60°), the merging electric field at the magnetopause must be below 0.8 mV m^{-1}.

This model uses the Swarm Level-2 Comprehensive Inversion (CI) algorithm (Sabaka et al., 2013). This method incorporates a bias mitigation scheme known as Selective Infinite Variance Weighting (SIVW), a new treatment for attitude error in satellite

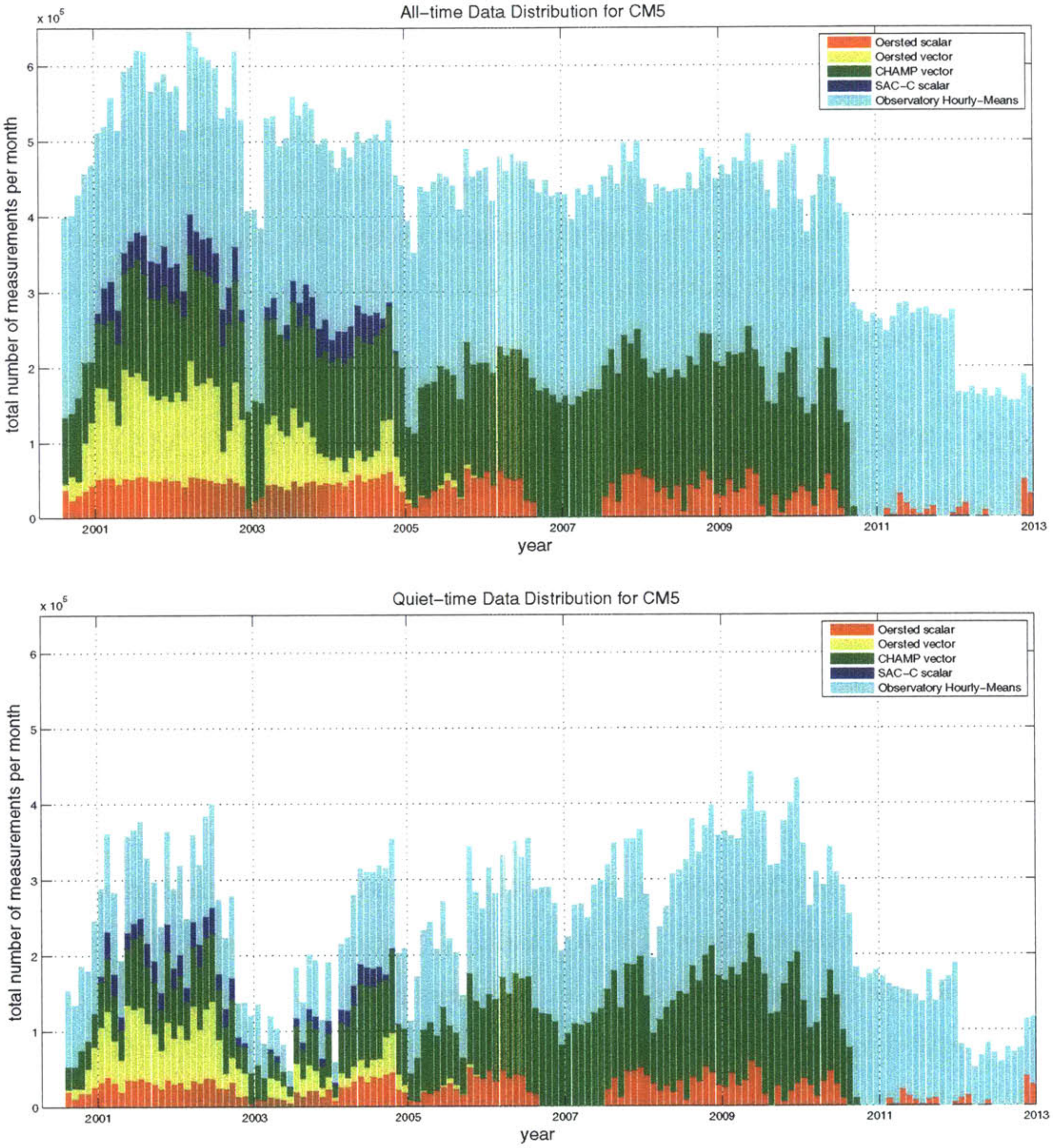

Figure 2-2: Reproduced from Sabaka et al. (2015), these stacked histograms show the number of measurements from all geomagnetic times (top panel), as well as only quiet geomagnetic times (bottom panel), used in deriving the CM5 model as a function of time. Note that both histograms are at the same scale. Measurement counts include all components where a scalar measuring counts as 1 measurement and a vector measurement counts as 3 measurements.

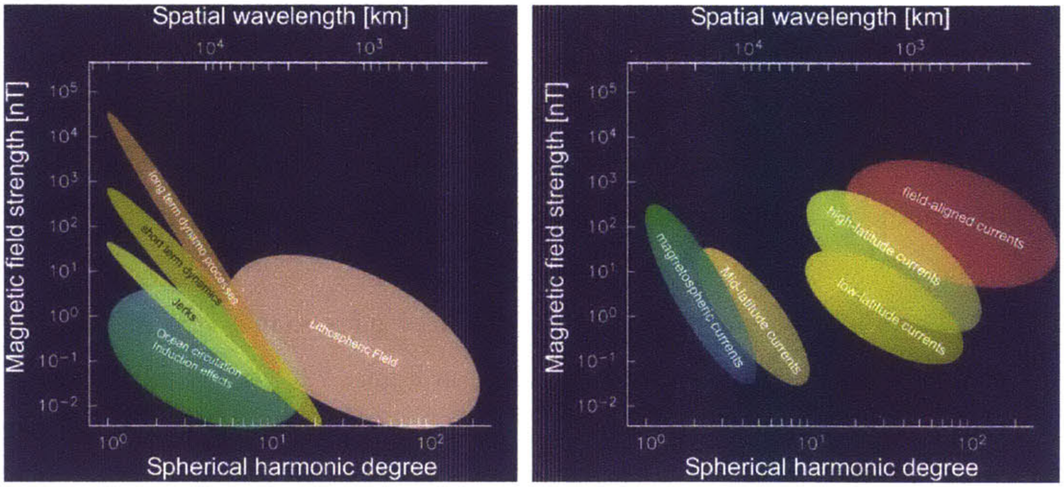

Figure 2-3: Reproduced from Friis-Christensen et al. (2006), these figures show the magnetic signal amplitude at *Swarm* orbital altitude from various geomagnetic sources as a function of spatial scale. Internal sources are shown on the left and external sources are shown on the right.

vector measurements, and the inclusion of 3-D conductivity for ionospheric induction. The CI method derives magnetic field models by parametrizing major magnetic field sources and then co-estimating them via least-squares (LS) to optimally separate the fields. The major field sources involved in this estimation include internal sources such as signals from the core and lithosphere (see Olsen et al. 2006; Thomson & Lesur 2007; Lesur et al. 2008, 2010; Thomson et al. 2010; Olsen et al. 2014), as well as the oceans. Major field external sources included ionospheric and magnetospheric current systems. In this way CM5 directly estimates the observed magnetic field due to different sources.

The M2 oceanic magnetic tide was extracted using quiet, nightside data. Its parametrization was included in CM5 as a simple internal spherical harmonic (SH) expansion where its potential at time $\triangle t$ and position $\mathbf{r}$ is:

$$V_{M2}(\triangle t, \mathbf{r}) = \mathcal{R}\left\{ a \sum_{n=1}^{36} \sum_{m=-n}^{n} \left(\frac{a}{r}\right)^{n+1} \tau_n^m Y_{n\omega}^m(\triangle t, \theta, \phi) \right\}, \tag{2.2.1}$$

where a is the Earth's radius (6371 km), τ_n^m are the complex Gaussian coefficients, and $Y_{n\omega}^m$ are the spherical harmonics for a frequency of $\omega = 2\pi/12.42060122$ rads/hr with time (t) rendered with respect to an arbitrary reference time, 00:00:00 1999 January 1 GMT, in order to fix the phase. To obtain conventional Greenwich phase used in ocean tidal literature, this phase must be adjusted by an angled of 35.71931° (equivalent to a time shift of 73.9 minutes).

The *Swarm* mission has been in orbit for a little more than a year and its data will also be incorporated into CM5. As shown in Figure 2-3, *Swarm* measurements should help more accurately isolate oceanic tidal signals and perhaps enable isolating the N2 and O1 tidal modes.

2.3 References

Friis-Christensen, E., Luhr, H., & Hulot, G., 2006. SWARM: A constellation to study the EarthâĂŹs magnetic field, *Earth Planets Space*, **58**, 351–358.

Kuvshinov, A. V., 2012. Deep Electromagnetic Studies from Land, Sea, and Space: Progress Status in the Past 10 Years, *Surveys in Geophysics*, **33**, 169–209.

Lesur, V., Wardinski, I., Rother, M., & Mandea, M., 2008. GRIMM: The GFZ Reference Internal Magnetic Model based on vector satellite and observatory data, *Geophysical Journal International*, **173**, 382–394.

Lesur, V., Wardinski, I., Hamoudi, M., & Rother, M., 2010. The second generation of the GFZ Reference Internal Magnetic Model: GRIMM-2, *Earth, Planets and Space*, **62**, 765–773.

Olsen, N. & Kotsiaros, S., 2011. Ch 2: Magnetic Satellite Missions and Data, in *Geomagnetic Observations and Models*, pp. 27–44, eds Mandea, M. & Korte, M., Springer Science+Business Media, New York.

Olsen, N. & Stolle, C., 2012. Satellite Geomagnetism, *Annual Review of Earth and Planetary Sciences*, **40**, 441–465.

Olsen, N., Toffner-Clausen, L., Sabaka, J. T., Brauer, P., Merayo, J. M., Lorgensen, J. L., Leger, J., Nielsen, O. V., Primdahl, F., & Risbo, T., 2003. Calibration of the Orsted vector magnetometer, *Earth Planets and Space*, **55**, 11–18.

Olsen, N., Lühr, H., Sabaka, T. J., Mandea, M., Rother, M., Tø ffner Clausen, L., & Choi, S., 2006. CHAOS - A model of the Earth's magnetic field derived from CHAMP, Ørsted, and SAC-C magnetic satellite data, *Geophysical Journal International*, **166**, 67–75.

Olsen, N., Lühr, H., Finlay, C. C., Sabaka, T. J., Michaelis, I., Rauberg, J., & Tø ffner clausen, L., 2014. The CHAOS-4 geomagnetic field model, *Geophysical Journal International*, **197**, 815–827.

Sabaka, T. J., Olsen, N., & Langel, R. a., 2002. A Comprehensive Model of the Near-Earth Magnetic Field: Phase 3, *Geophys. J. Int.*, **151**, 32–68.

Sabaka, T. J., Olsen, N., & Purucker, M. E., 2004. Extending comprehensive models of the Earth's magnetic field with Orsted and CHAMP data, *Geophysical Journal International*, **159**, 521–547.

Sabaka, T. J., Tø ffner Clausen, L., & Olsen, N., 2013. Use of the comprehensive inversion method for Swarm satellite data analysis, *Earth, Planets and Space*, **65**, 1201–1222.

Sabaka, T. J., Olsen, N., Tyler, R. H., & Kuvshinov, a., 2015. CM5, a pre-Swarm comprehensive geomagnetic field model derived from over 12 yr of CHAMP, Orsted, SAC-C and observatory data, *Geophysical Journal International*, **200**, 1596–1626.

Thomson, A. W. P. & Lesur, V., 2007. An improved geomagnetic data selection algorithm for global geomagnetic field modelling, *Geophysical Journal International*, **169**, 951–963.

Thomson, A. W. P., Hamilton, B., Macmillan, S., & Reay, S. J., 2010. A novel weighting method for satellite magnetic data and a new global magnetic field model, *Geophysical Journal International*, **181**, 250–260.

Tyler, R. H., Maus, S., & Lühr, H., 2003. Satellite observations of magnetic fields due to ocean tidal flow., *Science*, **299**(5604), 239–241.

Chapter 3

Geomagnetic induction numerical simulations

Here we discuss the global 3-D EM numerical simulations performed in order to quantitatively investigate the actual sensitivity of M2, N2 and O1 tidal signals to conductivity distributions at different depths. While M2 so far is the only ocean tidal mode to be isolated in satellite magnetic data, the success of Sabaka et al. (2015) gives us hope that it will also be possible to extract the N2 and O1 modes once *Swarm* data is incorporated into the Comprehensive Model.

3.1 Forward Simulation of the M2 EM Signals

We simulate EM signals due to the M2 (period of 12.4206 h), N2 (period of 12.6583 h) and O1 (period of 125.8193 h) oceanic tidal flow using the frequency-domain numerical solution described in Kuvshinov (2008). This solution computes the electric (**E**) and magnetic (**B**) fields excited by an electric source in spherical models of the Earth with a three-dimensional (3-D) distribution of electrical conductivity. Within this solution, Maxwell's equations in the frequency domain,

$$\frac{1}{\mu_0}\nabla \times \mathbf{B} = \sigma \mathbf{E} + \mathbf{j}^{ext} \tag{3.1.1}$$

and

$$\nabla \times \mathbf{E} = i\omega\mathbf{B} \ . \tag{3.1.2}$$

are reduced to an integral equation (IE) with a contracting kernel (e.g. Pankratov et al. 1995). Here $\mathbf{j}^{ext}$ is the complex-valued impressed current (in our case, $\mathbf{j}^{ext}$ is the electric current induced by the tidal flow), σ is the conductivity distribution of the model and μ_0 is the magnetic permeability of the free space. After solving the IE, the electric and magnetic fields at the observation points are calculated using Green's function formalism. For a detailed description of the 3-D EM simulation as applied to motionally-induced signals, see Kuvshinov & Olsen (2004) and Kuvshinov (2008). The impressed current, $\mathbf{j}^{ext}$, is calculated as

$$\mathbf{j}^{ext} = \sigma_w \left(\mathbf{U} \times \mathbf{B}^m\right) \ , \tag{3.1.3}$$

where $\sigma_w = 3.2$ S/m is the mean seawater conductivity, $\mathbf{U}$ is the complex-valued depth integrated velocity due to ocean tides, and $\mathbf{B}^m$ is the (ambient) magnetic field of internal (crustal and core) origin. Two assimilated tidal models of $\mathbf{U}$ were tried: the 0.25° × 0.25° resolution global tidal model TPX07.2 (Egbert & Erofeeva, 2002) and the 0.125°×0.125° resolution global tidal model HAMTIDE (shown in Fig. 3-1a-b) (Taguchi et al., 2014). The ambient magnetic field was derived from the World Magnetic Model (WMM) (Maus et al., 2010). Figure 3-1c shows the radial component of the main field which is determinative in specifying $\mathbf{j}^{ext}$. The 3-D model consisted of a thin spherical layer of laterally varying conductance at the Earth's surface (shown in Fig. 3-1d) and a radially symmetric spherical conductivity underneath (shown in Fig. 3-3). The surface conductance distribution was taken from Manoj et al. (2006) and accounts for the contributions from seawater and sediments. For the underlying laterally homogeneous spherical conductor, we used the model of Kuvshinov & Olsen (2006) as the default scenario (more explanation is provided in the following section). The 1° × 1° simulations were performed at the seafloor, sea-level, and satellite height (430 km altitude). Note that since we observed only negligible differences between the simulations which used the HAMTIDE and TPXO7.2 models (seen in Figures 3-2

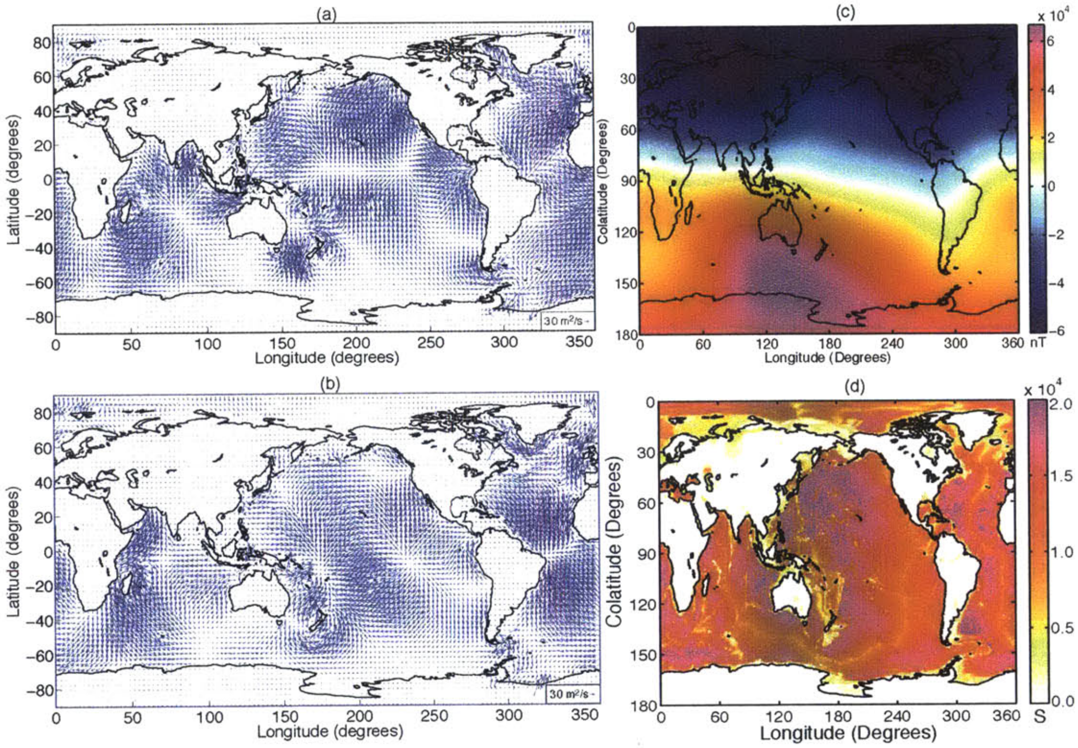

Figure 3-1: The a) real and b) imaginary velocity vectors for the depth-integrated M2 tidal velocities (m^2/s) produced by HAMTIDE, as well as c) the radial main field (nT) from WMM 2014 and d) global map of surface conductance (S).

and 3-5) for the tidal velocity, for the rest of our analysis we focus on the results that used the HAMTIDE model.

3.1.1 Comparison to CM5

Figure 3-4 shows the predicted M2 radial magnetic field and that recovered by CM5. One immediately sees that the observations and simulations agree very well. Further comparison may be made by looking at the power of each model. This was done using the R_n spectra. For the M2 tidal mode, the R_n spectrum is the mean-square field magnitude per degree over a sphere of radius r and over the M2 period, $T_{M2} =$ 12.42060122 hours (Sabaka et al., 2015). This corresponds to:

$$R_n(r) = (n+1)\left(\frac{a}{r}\right)^{2n+4}\left[\frac{1}{2}|\tau_n^0 n^2 + \sum_{m=1}^{n}\left(|\tau_n^m|^2 + |\tau_n^{-m}|^2\right)\right], \qquad (3.1.4)$$

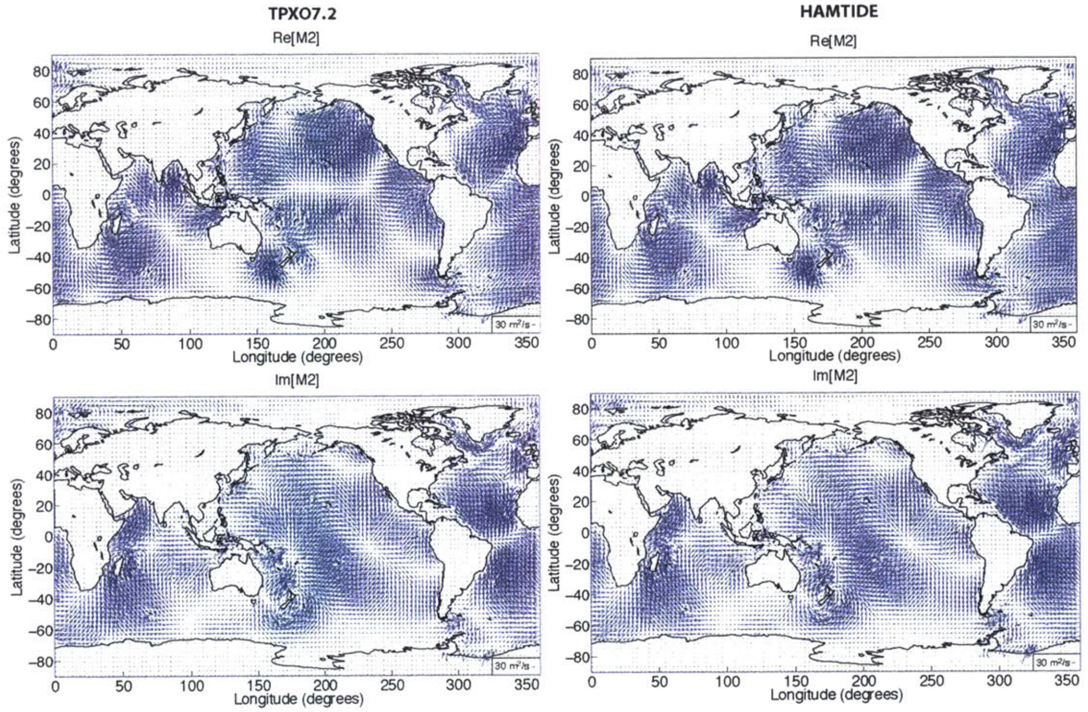

Figure 3-2: The real and imaginary velocity vectors for the depth-integrated M2 tidal velocities (m^2/s) produced by TPXO7.2 (left column) and HAMTIDE (right column).

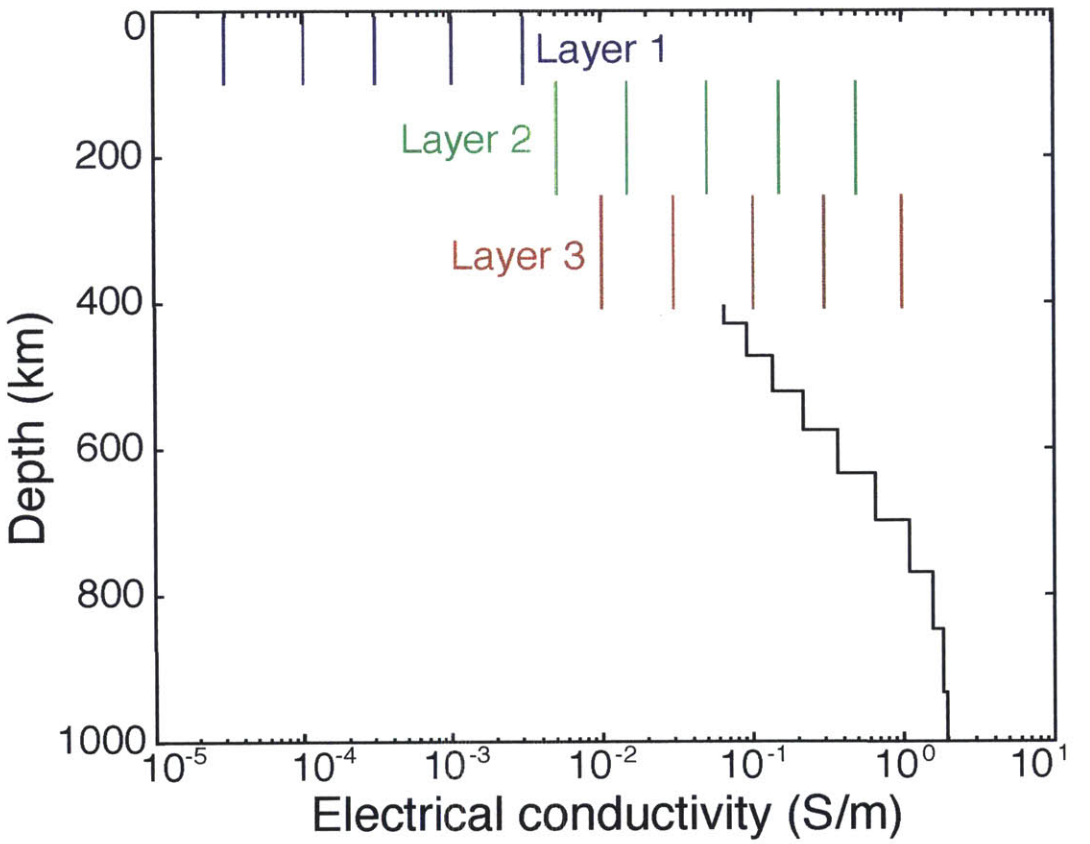

Figure 3-3: The five conductivity values used for layer 1 (navy blue), layer 2 (green) and layer 3 (red) are shown in vertical lines that span the layer's depth. Below the three layers, the black line depicts the conductivity profile from Kuvshinov & Olsen 2006.

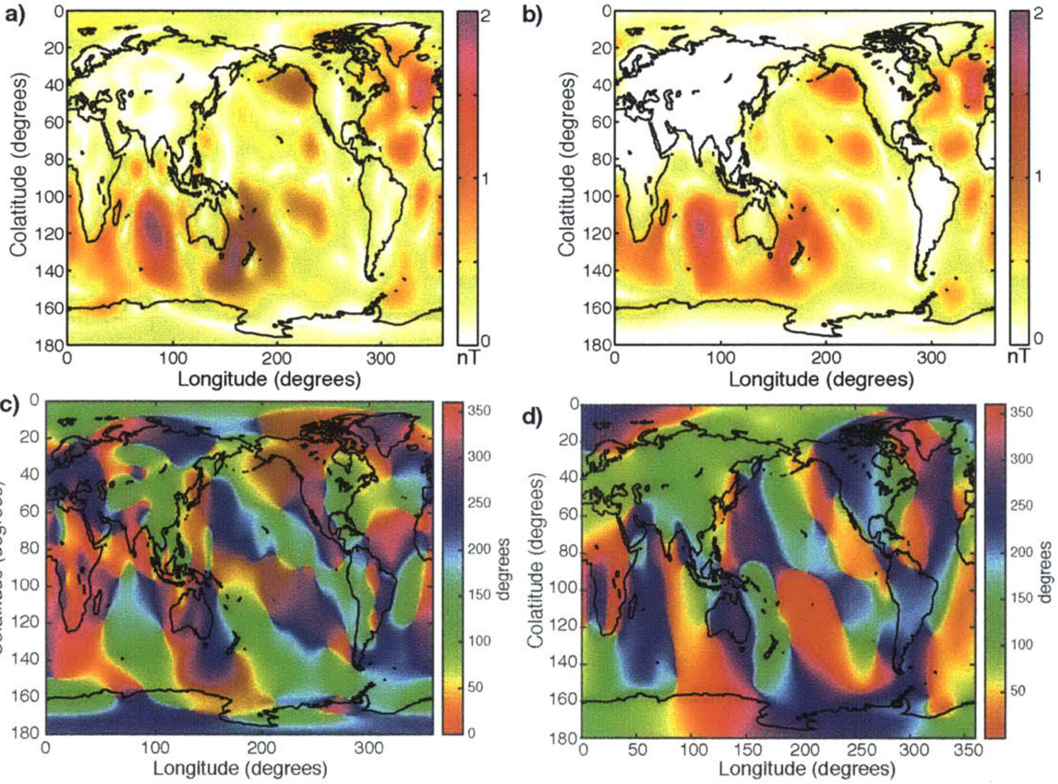

Figure 3-4: The amplitude of the M2 magnetic signals at satellite height from a) CM5 and b) our study's simulation using HAMTIDE for the tidal velocity source. The corresponding phases are shown in c) and d).

where τ_n^m is the gaussian coefficient for either the real field magnitude or imaginary field magnitude.

The R_n spectrum for CM5 and our model is shown in Figure 3-5. The observed signal has the most power, but the simulation using the HAMTIDE model has an insignificantly small edge over that using TPXO7.2 further supporting using HAMTIDE in the rest of this discussion. The simulations and observations both are well-behaved with power tapering off as degree increases.

Spherical harmonic transform of model output

A spherical harmonic transform is used to obtain the spherical harmonic coefficients (needed to produce the R_n spectrum) from the gridded values for the magnetic field

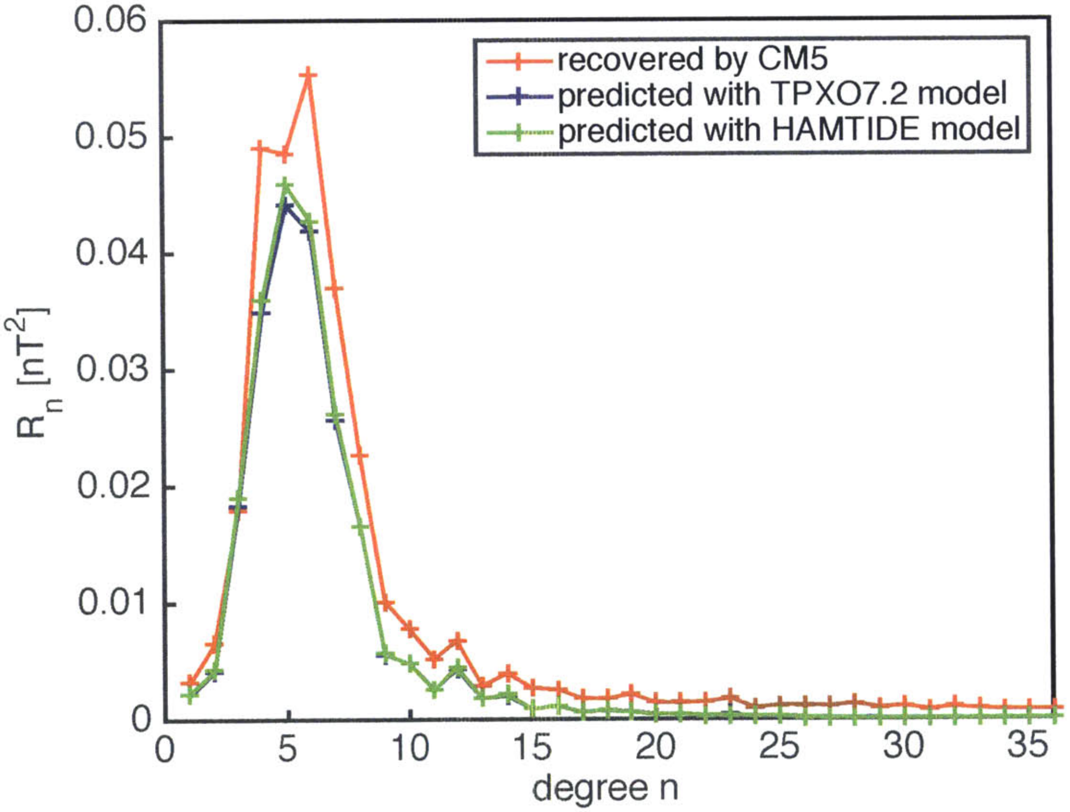

Figure 3-5: The R_n spectrum for CM5 and our model using HAMTIDE as the tidal velocity source (green) and TPXO7.2 as the tidal velocity source (blue).

models using HAMTIDE and TPXO7.2 as the tidal velocity source. Treating the model output as a function $f(\theta, \lambda)$ which is dependent on colatitude θ and longitude λ, the Fourier expansion of it on a sphere is given by:

$$f(\theta, \lambda) = \sum_{n=0}^{\infty} \sum_{|m| \leq n} f_{n,m} Y_n^m(\theta, \lambda), \tag{3.1.5}$$

where $Y_n^m(\theta, \lambda)$ are the spherical harmonics of degree n and order m. The spherical harmonic coefficients appearing in eq. 3.1.5 are obtained as inner products:

$$f_{n,m} = \int_S f(\theta, \lambda) \bar{Y}_n^m(\theta, \lambda) d\sigma, \tag{3.1.6}$$

where the overbar denotes the complex conjugate and $d\sigma$ denotes the standard rotation invariant on a sphere, $d\sigma = \sin\theta d\theta d\lambda$.

In geophysics, the spherical harmonic formulation is given as

$$f(\theta, \lambda) = \sum_{n=0}^{\infty} \sum_{m=0}^{n} [\tilde{c}_{nm} \cos m\lambda + \tilde{s}_{nm} \sin m\lambda] \tilde{P}_{nm}(\cos\theta), \tag{3.1.7}$$

where

$$\begin{pmatrix} \tilde{c}_{nm} \\ \tilde{s}_{nm} \end{pmatrix} = \frac{1}{4\pi} \int_S f(\theta, \lambda) \begin{pmatrix} \cos m\lambda \\ \sin m\lambda \end{pmatrix} \tilde{P}_{nm}(\cos\theta) d\sigma, \tag{3.1.8}$$

and $\tilde{P}_{nm}(\cos\theta)$ are the Schmidt seminormalized associated Legendre functions expressed in terms of spherical harmonics $Y_n^m(\theta, \lambda)$ (Blais, 2010).

3.2 Sensitivity analysis

A simple analysis was done to gauge the sensitivity of the M2, N2 and O1 tidal signals to changes in lithospheric and mantle conductivity. As specified in Table 3.1 and Figure 3-3, we varied the conductivity in the lithospheric layer (10-100 km) and the following two upper mantle layers (depths of 101-250 km and 251-410 km) to simulate magnetic and electric fields for cases of greater/lower conductivity value.

Table 3.1: Trial conductivities of lithosphere and upper mantle layers used during the simulation. Column marked by * contains conductivities recovered by Kuvshinov & Olsen (2006).

Depth of layer	Conductivity Values (S/m)				
	C1	C2	C3*	C4	C5
Layer 1: 10-100 km	0.003	0.001	0.0003	0.0001	0.00003
Layer 2: 101-250 km	0.5	0.16	0.05	0.016	0.005
Layer 3: 251-410 km	1	0.3	0.1	0.03	0.01

The depths of these layers were determined from seismic data– 100 km marks the base of the lithosphere and the transition zone starts at a depth of 410 km. We broke the upper mantle before the transition zone into two layers in a manner similar to Kelbert et al. (2008) and used 250 km as the midpoint between the two layers.

For each simulation run, only one layer's conductivity was varied while the other two layers were held at the default conductivity value from Kuvshinov & Olsen (2006) (cf. Table 3.1). In this way, the sensitivity of each oceanic tidal signal to the conductivity of a specific layer (i.e. sensitivity to depth) was determined.

Figures 3-6, 3-7, and 3-8 show the results of the sensitivity analysis at satellite height and at the seafloor for the M2, N2 and O1 tidal modes. The analysis was done for the radial magnetic field component and for the horizontal magnetic and electric field components. The plots show the Frobenius norm of the differences between the results obtained from conductivity scenario C1 versus scenarios C2, C3, C4 and C5 for each layer:

$$||S^{l,k}||_F = \left(\sum_{i,j} |F_{ij}^{l,k} - F_{ij}^{l,1}|^2 \right)^{1/2}, \tag{3.2.1}$$

where F denotes the corresponding field component, i, j labels grid points in or above oceanic regions, k represents the conductivity scenario ($C1, C2, C3, C4$, or $C5$) and l denotes the layer being analyzed (note that in the figures the results for the first, second and third layers are depicted by red, blue and black colors, respectively). In all layers, the range of conductivity values spanned two orders of magnitude. The upper row plots in Figs. 3-6, 3-7, and 3-8 show the results (i.e. the Frobenius norm) of the sensitivity analysis at satellite height. The Frobenius norm is the corresponding norm

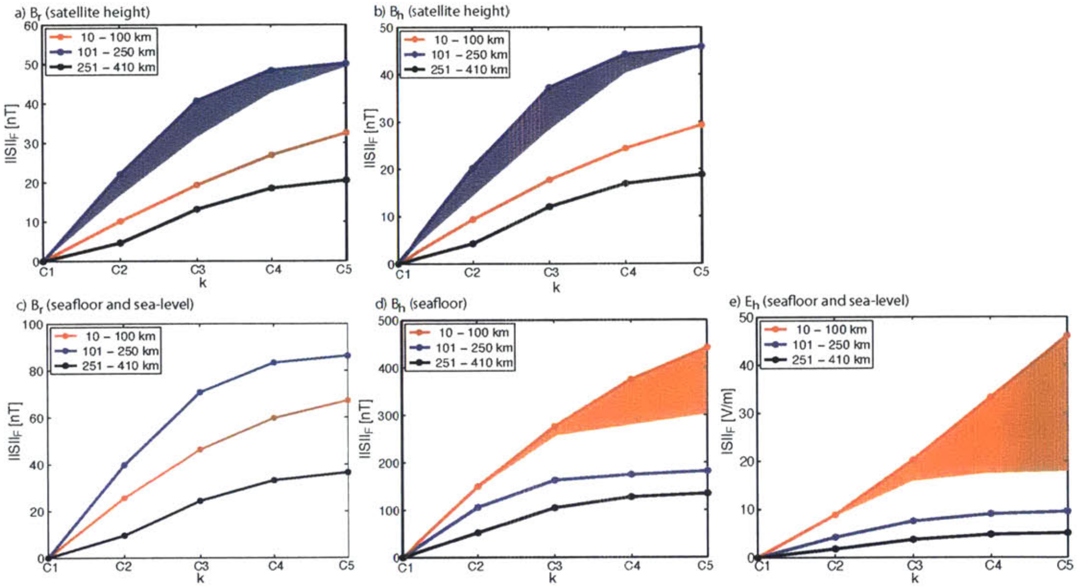

Figure 3-6: Results of the sensitivity analysis for the M2 tidal mode. Frobenius norms for a) the radial magnetic field component and b) the horizontal magnetic field component at satellite height, as well as c) the seafloor and sea-level radial magnetic field component, d) the seafloor horizontal magnetic field component and e) the seafloor and sea-level horizontal electric field. Regions that enable more unique inversions are highlighted.

for minimizing misfit across the global grid when doing inversions. The electric field at satellite height is not shown because this field (of telluric origin) is not measured by satellites. The maximum sensitivity is detected from conductivity changes in the first upper mantle layer (101-250 km), and the minimum sensitivity is due to changes in the second upper mantle layer (251-410 km).

3.2.1 M2 tidal mode sensitivity

The sensitivity of the M2 tidal mode flattens with decreasing conductivity, however, for all scenarios and layers changing the conductivity from C2 to C3 leads to a significant (two-fold) increase of $||S||_F$. For the M2 satellite magnetic signals, the sensitivity to the upper mantle layer (layer 2) is sufficiently stronger than the sensitivity of layers 1 and layers 3 that the total sensitivity of those two layers is less than that of layer 3. This is important for inversions since it helps decrease the possible degeneracies.

This shows that M2 satellite magnetic signals can be used to probe the conductivity of the lithosphere and upper mantle. The overall behavior of $||S||_F$ for radial (Fig. 3-6a) and horizontal (Fig. 3-6b) magnetic field components at satellite height is very similar. This, in particular, means that above the Earth the horizontal magnetic field component does not add any new information about the Earth's conductivity.

The lower row of plots in Fig. 3-6 shows the results of the sensitivity analysis at the seafloor. Note that the radial magnetic field and horizontal electric field components are the same at sea-level and at the seafloor. The behavior of $||S||_F$ in the radial component at satellite height and at sea-level (cf. left-most plots) is very similar, with the only difference being that $||S||_F$ at sea-level is about two times larger than $||S||_F$ at satellite height. Because of this, the seafloor is relatively more sensitive to all three layers and no layer's sensitivity exceeds the summation of the other layers' sensitivities.

Dramatic changes in $||S||_F$ occur in the horizontal magnetic field component at the sea-floor compared with at satellite height. First, $||S||_F$ at the sea-floor is about ten times larger than $||S||_F$ at satellite height. Secondly, the horizontal magnetic field appears to be most sensitive to conductivity changes in the lithospheric layer (10-100 km). Beyond $k = C3$, the sensitivity to the lithospheric layer is much greater than the other two layer's minimizing inversion degeneracies. The same is true for the horizontal electric field, as it shows even larger sensitivity to lithospheric conductivity. This suggests that the seafloor magnetic and electric field data (such as those used by Toh et al. 2006; Baba et al. 2010, 2013; Schnepf et al. 2014) could provide complementary insights on lithospheric conductivity.

3.2.2 N2 tidal mode sensitivity

The sensitivity of the N2 tidal mode to the upper mantle layers flattens with decreasing conductivity, however for the lithospheric layer, the sensitivity instead increases more sharply. Changing the conductivity from C2 to C3 leads to a significant (two-fold) increase of $||S||_F$ for the upper mantle layers, whereas the lithospheric layer increases $||S||_F$ more sharply during transitions of C3 to C4 or C4 to C5. Because of

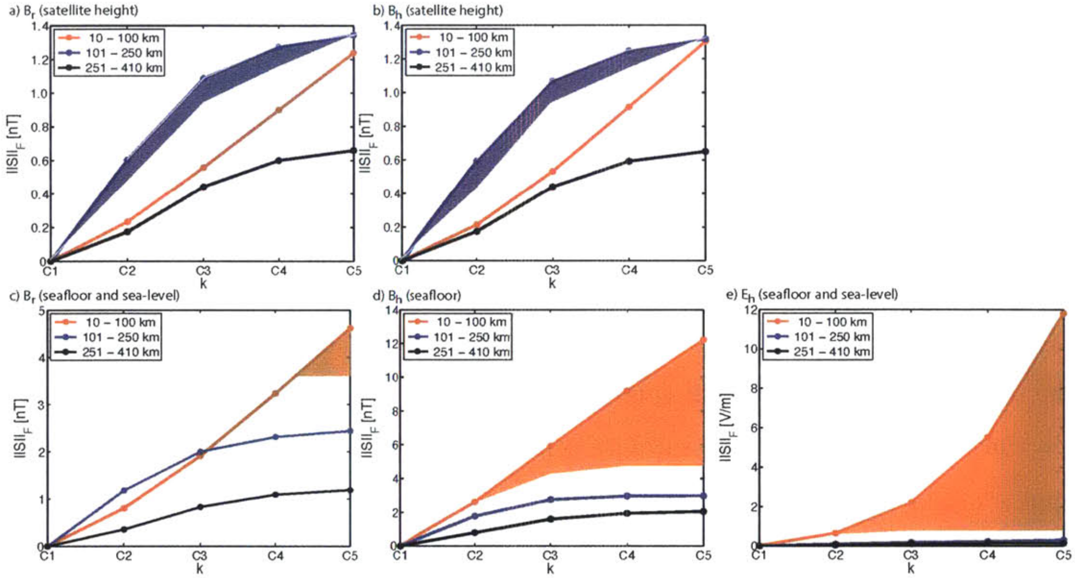

Figure 3-7: Results of the sensitivity analysis for the N2 tidal mode. Frobenius norms for a) the radial magnetic field component and b) the horizontal magnetic field component at satellite height, as well as c) the seafloor and sea-level radial magnetic field component, d) the seafloor horizontal magnetic field component and e) the seafloor and sea-level horizontal electric field. Regions that enable more unique inversions are highlighted.

this, unlike for M2, at satellite height the sensitivity lines for layers 1 and 2 eventually cross each other causing inversion degeneracies to increase as conductivity decreases.

The overall behavior of $||S||_F$ for radial (Fig. 3-7a) and horizontal (Fig. 3-7b) magnetic field components at satellite height is very similar. This supports the previously discussed notion that above the Earth the horizontal magnetic field component does not add any new information about the Earth's conductivity. If extractable from satellite data, these results suggest the N2 satellite magnetic signals may be used to probe LUM conductivity.

As before, the lower row of plots in Fig. 3-7 show the results of the sensitivity analysis at the seafloor. The behavior of $||S||_F$ in the radial component at satellite height and at sea-level (cf. left-most plots) is very different for the lithospheric layer: at sea-level it increases much more rapidly than at satellite height and for C4 and C5 it is has larger $||S||_F$ values than the upper mantle layer does. However, because the lithospheric sensitivity lines are so close to those of the upper mantle, it is not until conductivity values become much smaller (beyond $k = C4$) that more unique solutions may be determined. For the horizontal component, this change is even more dramatic and the lithospheric layer has the largest $||S||_F$ for each k value, with values larger than the summation of the upper mantle layers beyond $k = C2$. In both cases, the amplitude of $||S||_F$ is an order of magnitude larger at the seafloor/sea-level than at satellite height. The horizontal seafloor electric field is also most sensitive to lithospheric conductivity.

While the N2 tidal signal has yet to be successfully isolated is satellite magnetic data, it has previously been successfully isolated at seafloor and coastal stations (see Maus & Kuvshinov 2004; Kuvshinov et al. 2006; Love & Rigler 2014; Schnepf et al. 2014) and these seafloor magnetic and electric field data could provide complementary insights on lithospheric conductivity.

3.2.3 O1 tidal mode sensitivity

For the O1 tidal mode, at satellite height (Fig. 3-8a-b) the C3-C5 cases are dominated by variations in lithospheric conductivity. The behavior of $||S||_F$ for the upper mantle

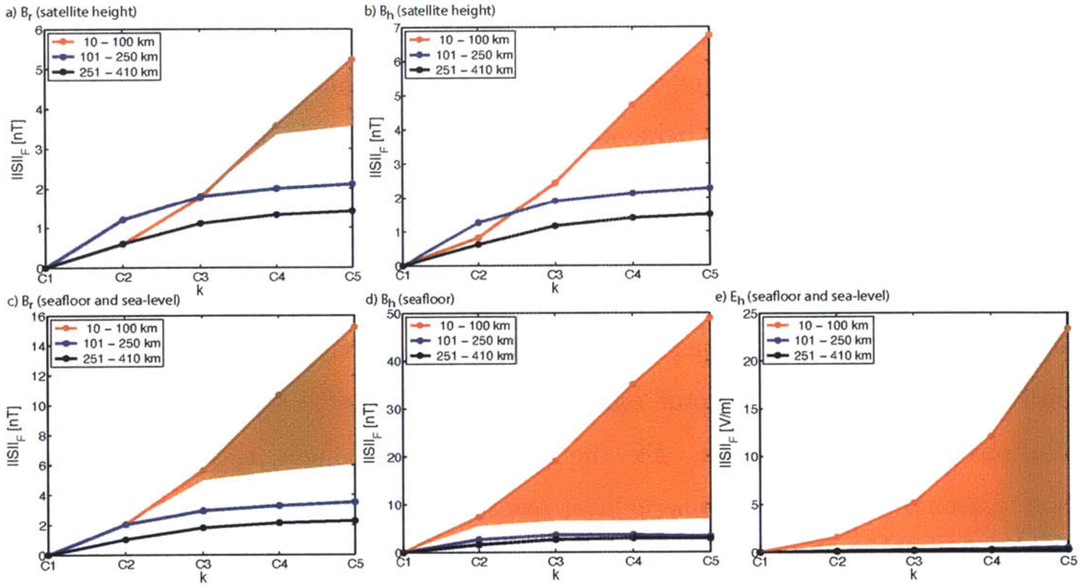

Figure 3-8: Results of the sensitivity analysis for the O1 tidal mode. Frobenius norms for a) the radial magnetic field component and b) the horizontal magnetic field component at satellite height, as well as c) the seafloor and sea-level radial magnetic field component, d) the seafloor horizontal magnetic field component and e) the seafloor and sea-level horizontal electric field. Regions that enable more unique inversions are highlighted.

layers is similar at both satellite height and at seafloor/sea-level for all components: it has the largest increase between C1 and C2 and then levels off with decreasing conductivity. At the seafloor and sea-level, the lithosphere has similar shape as at satellite height: $||S||_F$ steadily increases with the largest gains between C3 and C4 for the magnetic field cases and between C4 and C5 for the horizontal electric field. At the seafloor (and sea-level), the lithospheric $||S||_F$ values reach an order of magnitude larger than at satellite height, causing all three components to be most sensitive to the lithosphere. Because the upper mantle layers level off so rapidly, all components of the O1 field lend themselves to lower-degeneracy inversions.

Like the N2 tidal mode, the O1 mode has so far only been detected in seafloor and coastal stations (see Maus & Kuvshinov 2004; Kuvshinov et al. 2006; Love & Rigler 2014; Schnepf et al. 2014). This sensitivity analysis suggests seafloor magnetic and electric field data could provide complementary insights on lithospheric conductivity, as could satellite data should the signal be obtained from *Swarm* data.

3.3 Discussion

A very surprising result of the sensitivity analysis is that the satellite signals of the M2 tidal mode are more sensitive to the upper mantle whereas those from the O1 tidal mode (which has a period roughly twice as long as the M2 tidal mode) are instead most sensitive to the shallower lithosphere. This is directly opposite what would be expected from only considering the notion of skin depth (see eqn. 1.3.1). To understand this counter-intuitive result, it is helpful to look at the map of differences, $F_{ij}^{l,k} - F_{ij}^{l,1}$ from eqn. 3.2.1. Figures 3-9, 3-10 and 3-11 show the differences for each layer and each k value for, respectively, the M2, N2 and O1 tidal modes' radial component at satellite height.

Looking at Fig. 3-11, it can be seen that changing the lithospheric conductivity mostly causes O1 field variations in polar regions. As shown in Fig. 3-1c, the Earth's main field is strongest in the polar areas – including the Northern regions where O1's lithospheric changes are largest. The surface conductivity (Fig. 3-1d) of this region

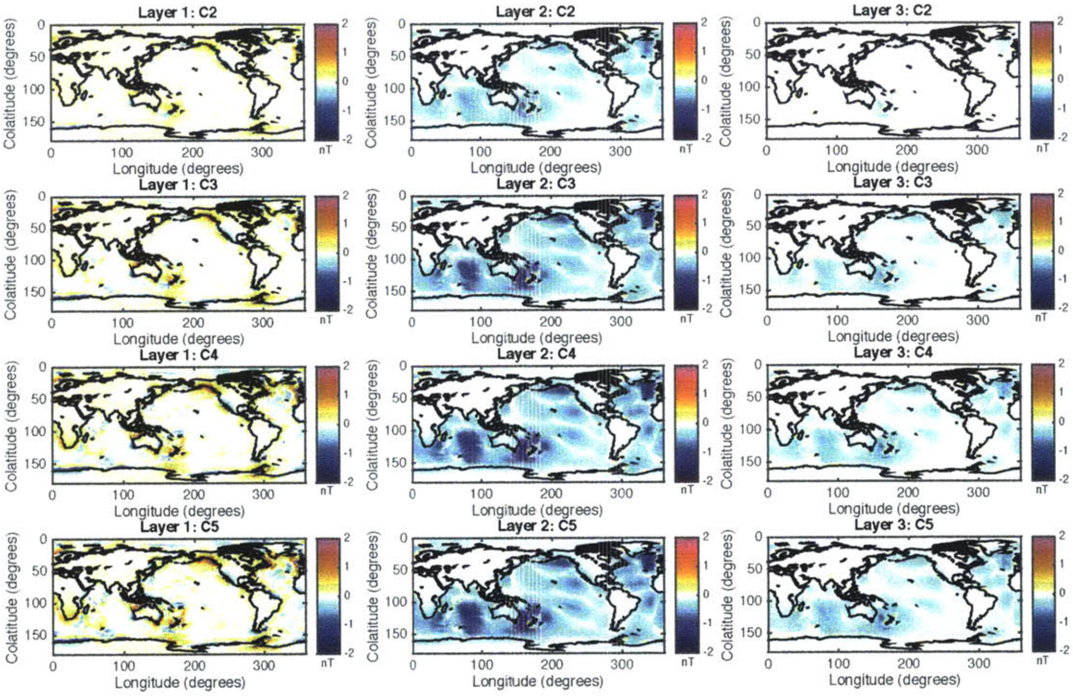

Figure 3-9: Maps of the differences ($F_{ij}^{l,k} - F_{ij}^{l,1}$ from eqn. 3.2.1) computed in the sensitivity analysis of each layer for $k = C2, C3, C4$ and $C5$ for the M2 tidal mode's radial component at satellite altitude.

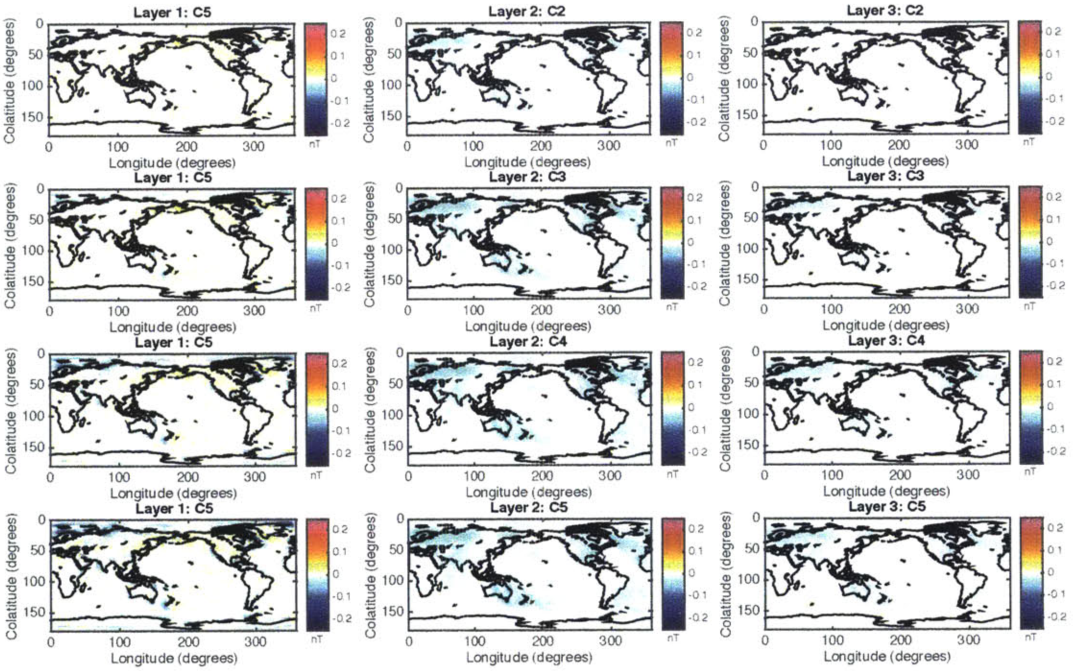

Layer 1: C5
Layer 2: C2
Layer 3: C2
Layer 1: C5
Layer 2: C3
Layer 3: C3
Layer 1: C5
Layer 2: C4
Layer 3: C4
Layer 1: C5
Layer 2: C5
Layer 3: C5

Figure 3-10: Maps of the differences ($F_{ij}^{l,k} - F_{ij}^{l,1}$ from eqn. 3.2.1) computed in the sensitivity analysis of each layer for $k = C2, C3, C4$ and $C5$ for the N2 tidal mode's radial component at satellite altitude.

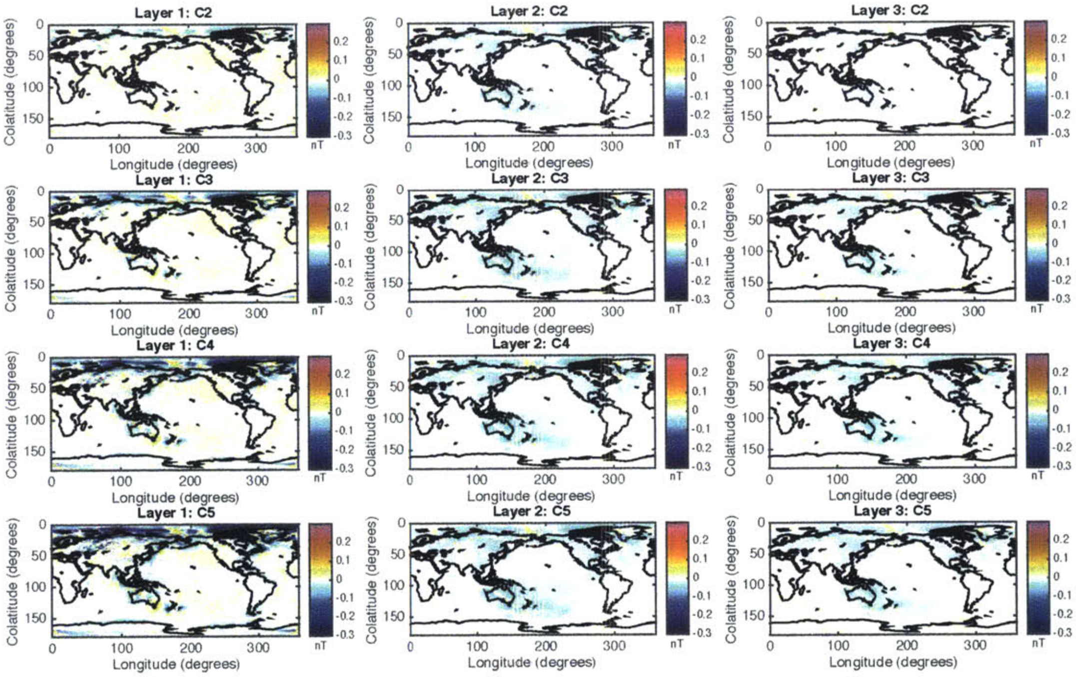

Figure 3-11: Maps of the differences ($F_{ij}^{l,k} - F_{ij}^{l,1}$ from eqn. 3.2.1) computed in the sensitivity analysis of each layer for $k = C2, C3, C4$ and $C5$ for the O1 tidal mode's radial component at satellite altitude.

also is markedly more resistive than other areas causing the shallower field to be more sensitive to smaller changes in lithospheric conductivity (in regions where the surface conductivity is greater, it may compensate for smaller lithospheric conductivity values). For the deeper layers, the largest O1 variations are spread more in regions of the Pacific where the main field's strength is not as strong (and hence neither are the induced O1 fields) and the surface is generally more conductive. This explains why O1 would have the greatest sensitivity to the lithospheric signal.

For M2 and N2, the largest differences are more spread out. Interestingly, M2's layer 2 has its largest variations in field strength within the Indian and Southern ocean near the southern geomagnetic pole. In this region, the geomagnetic field is even stronger than at the North pole so the induced M2 signals are much stronger. This explains why despite having the shortest period, the M2 tidal mode's satellite signals are most sensitive to the upper mantle layer.

3.3.1 Influence of electromagnetic noise

Our model produces negligible differences in the sensitivity analysis when using TPXO7.2's tidal velocity model versus HAMTIDE. Instead, the sensitivity analysis is likely to vary depending on how pure the isolated tidal EM signal is. The M2 signal isolated from CM5 has a noise level of 0.2 nT (Sabaka et al., 2015). The signal from CM5 was estimated assuming ionospheric nighttime signals are negligible. If we instead allow ionospheric signals to add up to 0.3 nT of noise, this raises the total noise level to 0.5 nT. To determine how much noise would influence the results, noise randomly selected between 0 and 0.2 nT (for the case where the ionosphere is truly negligible) and 0 and 0.5 nT were added to each grid in the difference matrix $|F_{ij}^{l,k} - F_{ij}^{l,1}|$ from eqn. 3.2.1 for the radial and horizontal magnetic fields at satellite height. The results of this are shown in Figure 3-12.

Adding noise dramatically alters the sensitivity of the satellite detected M2 signals. In the case of only adding up to 0.2nT of noise (Fig. 3-12a-b), the radial component is now almost equally sensitive to the lithospheric and upper mantle. With noise ranging up to 0.5 nT (Fig. 3-12c-d), the radial component is most sensitivity to the

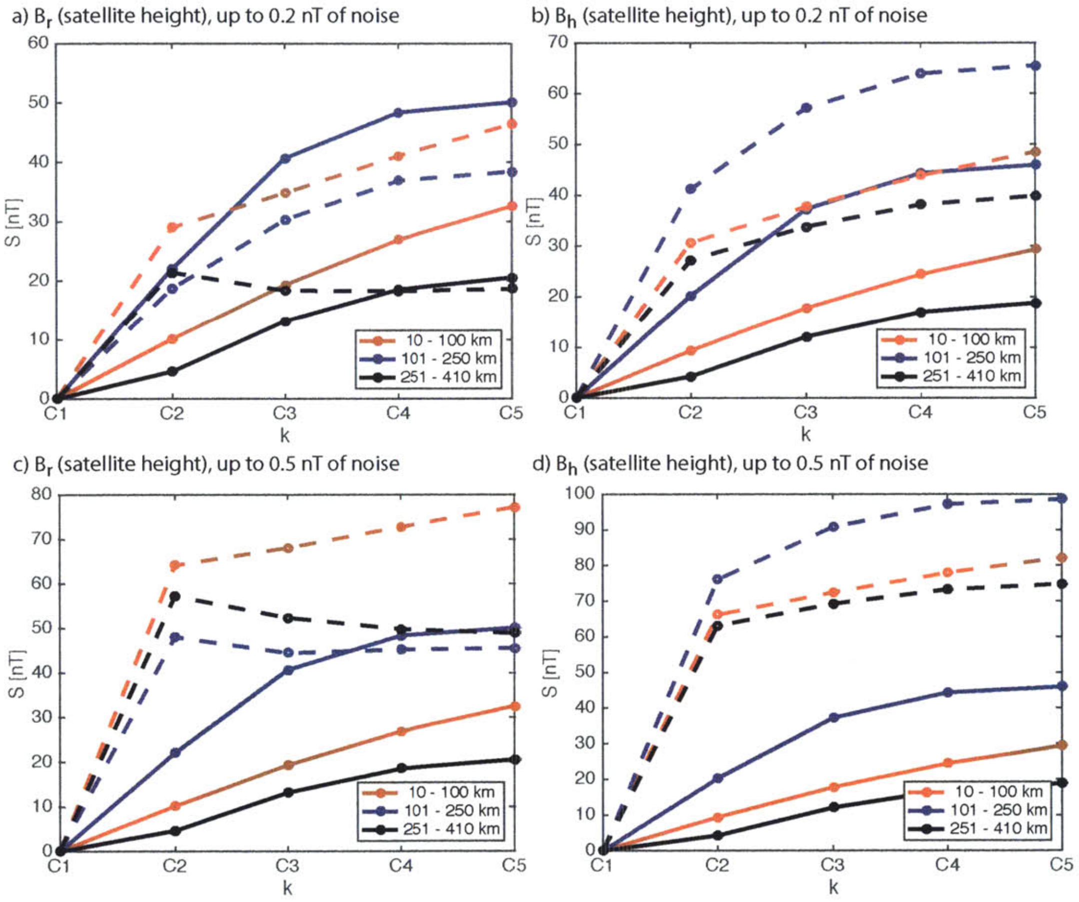

Figure 3-12: The same as Figure 3-6a-b, except for the additional dotted lines denoting the results for the sensitivity analysis when random noise is added to the grid of the differences ($|F_{ij}^{l,k} - F_{ij}^{l,1}|$ from eqn. 3.2.1). The top row noise ranging from 0 to 0.2nT and in the bottom row the noise ranges from 0 to 0.5 nT.

lithosphere and as conductivity continues to decrease the lithospheric sensitivity likely would become larger than the total upper mantle sensitivity. In both noise scenarios, the sensitivity most rapidly changes between C1 and C2. After C2, for up to 0.2 nT of noise, the top two layers' sensitivity continues to slowly climb upwards whereas the layer 3 values decrease and flatten. For up to 0.5 nT of noise, both upper mantle layers decrease and flatten after C2 while the lithospheric layer continues to slowly increase.

In both scenarios, the horizontal component's results differ from the radial components' and become much more sensitive to the first upper mantle layer (although its sensitivity is not great enough to exceed the summation of the other two layers'). The sensitivity now increases most rapidly between C1 and C2, and then proceeds to level off. Increasing the level of noise increases the difference between the sensitivity values with noise and those without, but does not alter the shape of the sensitivity curves.

While the sensitivity analysis figures are different with noise incorporated, they still suggest satellites may be used to probe the conductivity of the lithosphere and upper mantle. However, because these results lead to greater degeneracies in the inverse solutions, it would be best to incorporate seafloor data in the inversions. The noise at the seafloor is expected to be < 0.1 enabling reliable tidal signal extraction (Schnepf et al., 2014) and negligibly altering the sensitivity analysis results for the seafloor components. Using seafloor data is also very important because the N2 and O1 signals so far are not above the satellite noise thresholds.

3.4 Conclusions

This numerical work provides estimates of the magnetic field produced by the oceanic M2, N2 and O1 tides as detected at satellite height, at sea-level and at the seafloor. Our simulations of M2 closely match the observed M2 magnetic field amplitudes estimated from CM5. Our sensitivity analysis of these three oceanic tidal amplitudes suggests it will be promising for future studies to use already-isolated satellite M2 oceanic signals to probe lithospheric and upper mantle conductivity. Our results also suggest seafloor data of M2, N2 and O1 can provide complementary details to better determine lithospheric conductivity.

3.5 References

Baba, K., Utada, H., Goto, T.-N., Kasaya, T., Shimizu, H., & Tada, N., 2010. Electrical conductivity imaging of the Philippine Sea upper mantle using seafloor magnetotelluric data, *Physics of the Earth and Planetary Interiors*, **183**(1-2), 44–62.

Baba, K., Tada, N., Zhang, L., Liang, P., Shimizu, H., & Utada, H., 2013. Is the electrical conductivity of the northwestern Pacific upper mantle normal?, *Geochemistry, Geophysics, Geosystems*, **14**(12), 4969–4979.

Blais, J. A. R., 2010. Discrete Spherical Harmonic Transforms for Equiangular Grids of Spatial and Spectral Data, *Journal of Geodetic Science*, **1**, 9–16.

Egbert, G. D. & Erofeeva, S. Y., 2002. Efficient Inverse Modeling of Barotropic Ocean Tides, *Journal of Atmospheric and Oceanic Technology*, **19**, 183–204.

Kelbert, A., Egbert, G. D., & Schultz, A., 2008. Non-linear conjugate gradient inversion for global EM induction: Resolution studies, *Geophysical Journal International*, **173**(2), 365–381.

Kuvshinov, A. & Olsen, N., 2004. 3-D modelling of the magnetic fields due to ocean tidal flow, in *CHAMP Mission Results II*, pp. 359–365, Springer, Berlin.

Kuvshinov, A. & Olsen, N., 2006. A global model of mantle conductivity derived from 5 years of CHAMP, Ørsted, and SAC-C magnetic data, *Geophysical Research Letters*, **33**(18), L18301.

Kuvshinov, A., Junge, A., & Utada, H., 2006. 3-D modelling the electric field due to ocean tidal flow and comparison with observations, *Geophysical Research Letters*, **33**(6), L06314.

Kuvshinov, A. V., 2008. 3-D Global Induction in the Oceans and Solid Earth: Recent Progress in Modeling Magnetic and Electric Fields from Sources of Magnetospheric, Ionospheric and Oceanic Origin, *Surveys in Geophysics*, **29**(2), 139–186.

Love, J. J. & Rigler, E. J., 2014. The magnetic tides of Honolulu, *Geophysical Journal International*, **197**, 1335–1353.

Manoj, C., Kuvshinov, A., Maus, S., & Luhr, H., 2006. Ocean circulation generated signals, *Earth Planets Space*, **58**, 429–437.

Maus, S. & Kuvshinov, A., 2004. Ocean tidal signals in observatory and satellite magnetic measurements, *Geophysical Research Letters*, **31**, L15313.

Maus, S., Macmillan, S., McLean, S., Hamilton, B., Thomson, A., Nair, M., & Rollins, C., 2010. The US/UK World Magnetic Model for 2010-2015.

Pankratov, O., Avdeev, D., & Kuvshinov, A., 1995. Electromagnetic field scattering in a homogeneous Earth: a solution to the forward problem., *Phys. Solis. Earth*, **31**, 201–209.

Sabaka, T. J., Olsen, N., Tyler, R. H., & Kuvshinov, a., 2015. CM5, a pre-Swarm comprehensive geomagnetic field model derived from over 12 yr of CHAMP, Orsted, SAC-C and observatory data, *Geophysical Journal International*, **200**, 1596–1626.

Schnepf, N. R., Manoj, C., Kuvshinov, A., Toh, H., & Maus, S., 2014. Tidal signals in ocean bottom magnetic measurements of the Northwestern Pacific: Observation versus prediction, *Geophysical Journal International*, **198**(2), 1096–1110.

Taguchi, E., Stammer, D., & Zahel, W., 2014. Inferring deep ocean tidal energy dissipation from the global high-resolution data-assimilative HAMTIDE model, *Journal of Geophysical Research: Oceans*, **119**, 4573–4592.

Toh, H., Hamano, Y., & Ichiki, M., 2006. Long-term seafloor geomagnetic station in the northwest Pacific : A possible candidate for a seafloor geomagnetic observatory, *Earth Planets Space*, **58**, 697–705.

Chapter 4

Conclusions and future work

4.1 Conclusions

Our sensitivity analysis of oceanic M2, N2 and O1 tidal EM signals suggests it will be promising for future studies to use oceanic tidal signals to probe lithospheric and upper mantle conductivity. Our analysis also suggests that seafloor magnetic and electric data can provide complementary details to better determine lithospheric conductivity. We found that the satellite M2 and N2 signals are best suited for probing the upper mantle, whereas the O1 signals are most sensitive to the lithosphere. While this may seem contrary to the skin depth principle, the nature of each tidal mode's induction in the Earth's main field explains why their sensitivity follows oppositely with depth.

Our analysis shows that satellite or ionospheric noise does not limit the ability to use satellite detected M2 signals for probing lithospheric and mantle conductivity. However, to produce more detailed inversion it would be best to incorporate seafloor data. This is especially true since the N2 and O1 tidal modes so far are very well detected at the seafloor, but not at satellite height.

We have to stress that there are some strong advantages of working with oceanic tidal signals. First, the spatial structure of the tidal source is determined more accurately compared with the ionospheric Sq source. Secondly, in contrast to Sq signals, the oceanic tidal signals – being of gravitational origin – do not undergo day-to-day and seasonal variability and, moreover, do not depend on solar activity as the Sq signals do. Due to the direct galvanic coupling of the source (electric currents in the ocean) with the subsurface structures, tidal signals are more sensitive than Sq signals to shallower and less conductive structures. Sq signals instead undergo inductive coupling between the source and subsurface. However, working with tidal signals also has some shortcomings, for example, in contrast to the global Sq source, the tidal source is confined only to oceanic regions. Arguably, because there is a relative lack of observatories in oceanic regions, this disadvantage is in fact filling in a needed knowledge gap in investigating the oceanic lithosphere and upper mantle.

4.2 Future work

4.2.1 Inversions

The next natural step of the research would be inverting the recovered tidal signals (as well as those yet to be recovered from Swarm data) in terms of lithospheric/upper-mantle conductivity (either in the frame of a 1-D or 3-D model). Inversions are a minimization-problem where we aim to determine which conductivity model minimizes the differences between observations and model results.

For calculating model results, we will be using the same forward-modeling scheme. We will then follow a method similar to Koch & Kuvshinov (2015) where the conductivity recovery is formulated as the minimization of a penalty function:

$$\phi(\mathbf{m}, \lambda) = \phi_d(\mathbf{m}) + \lambda \phi_R(\mathbf{m}), \tag{4.2.1}$$

where $\mathbf{m} = (\log \sigma_1, \log \sigma_2, \ldots, \log \sigma_N)$ is a vector containing the conductivities in the layers which comprise the inverse modeling domain, λ is the regularization parameter, $\phi_R(\mathbf{m})$ is the regularization term and $\phi_d(\mathbf{m})$ is the data misfit. The methods of the inverse approach are covered in detail in Kuvshinov & Semenov (2012) and Koch &

Kuvshinov (2013). For this problem, the data misfit $\phi_d(\mathbf{m})$ is:

$$\phi_d(\mathbf{m}) = ||F^m - F^e||^2 \tag{4.2.2}$$

where F^m and F^e respectively are the modeled and experimental components of the magnetic field for a given tidal signal and the misfit is the norm over the grid points.

4.2.2 Improving the model for 3-D inversions

Some improvements to the model are needed before 3-D inversions can be done. Our model assumes one value for ocean conductivity, when conductivity in fact spatially and temporally varies. Figures 4-1 and 4-2 show the spatial variations in salinity and temperature for each season. Conductivity depends on both of these parameters and consequently also will change. Our model already uses a 2-D surface conductance map, so it should not be too challenging to also incorporate a 2-D ocean conductuctivity map.

Many scientists are also interested in using satellite-detected magnetic fields to study the ocean. Incorporating 2-D or 3-D ocean conductivity maps into our model could also allow us to probe Earth's ocean.

4.3 References

Koch, S. & Kuvshinov, A., 2013. Global 3-D EM inversion of Sq variations based on simultaneous source and conductivity determination: Concept validation and resolution studies, *Geophysical Journal International*, **195**, 98–116.

Koch, S. & Kuvshinov, A., 2015. Regional large scale 3-D EM inversion of ground based geomagnetic Sq data . A concept and results from the analysis of the AWAGS data, *Geophysical Journal International*, **200**, 1284–1296.

Kuvshinov, A. & Semenov, A., 2012. Global 3-D imaging of mantle electrical conductivity based on inversion of observatory C-responses-I. An approach and its verification, *Geophysical Journal International*, **189**, 1335–1352.

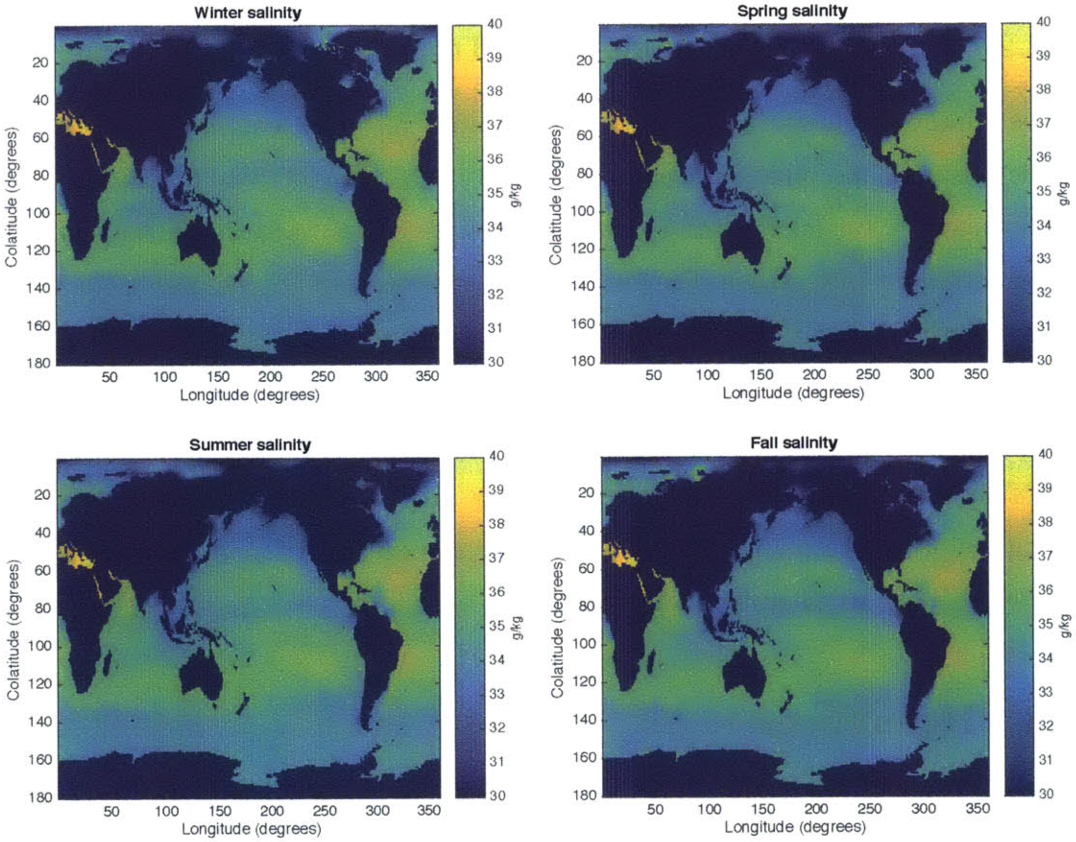

Figure 4-1: Global seasonal salinity variations.

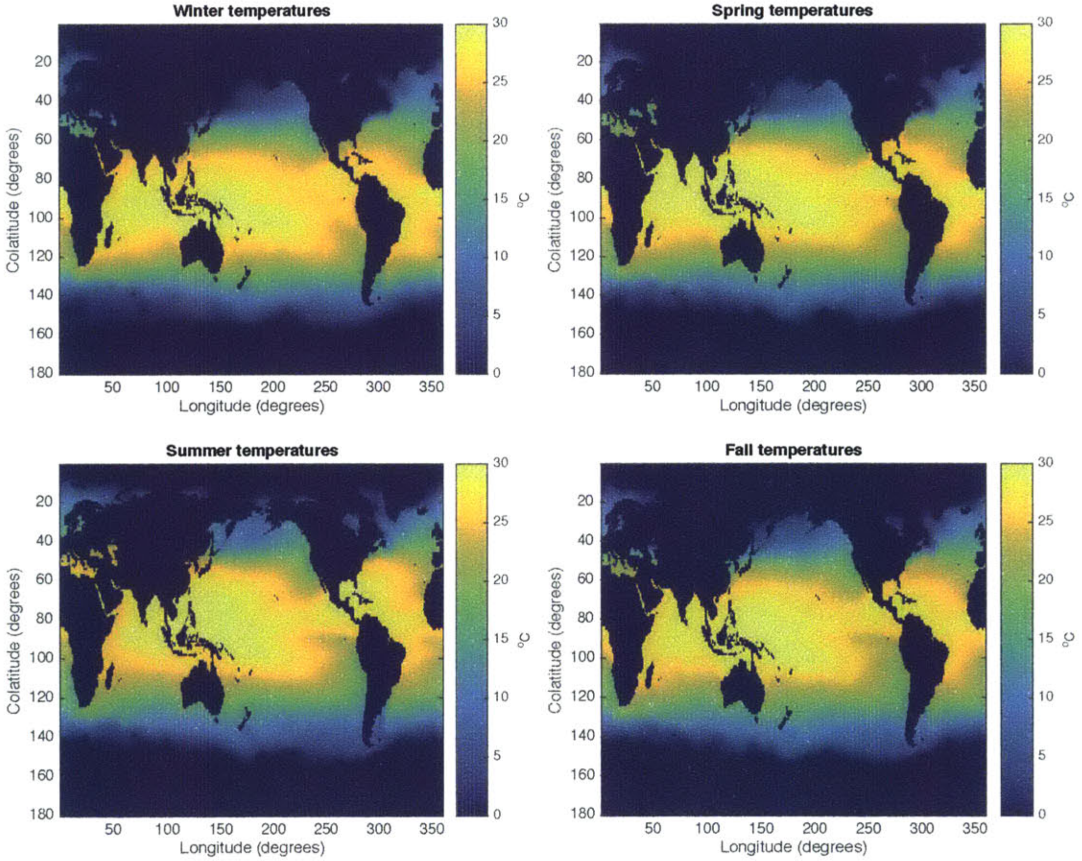

Figure 4-2: Global seasonal temperature variations.